COMPUTER METHODS IN BIOMECHANICS AND BIOMEDICAL ENGINEERING

Publisher- Taylor and Francis (USA)
Print ISSN: 1025-5842; Online ISSN: 1476-8259, impact factor = 1.974

Accepted February 11th 2020

COMPUTATIONAL FLUID DYNAMIC SIMULATION OF TWO-FLUID NON-NEWTONIAN NANO-HEMODYNAMICS THROUGH A DISEASED ARTERY WITH A STENOSIS AND ANEURYSM

Ankita Dubey[a], B. Vasu[a] *, O. Anwar Bég[b], Rama S R Gorla[c] and **Ali Kadir[b]**

[a]Department of Mathematics, Motilal Nehru National Institute of Technology Allahabad, Prayagraj, Uttar Pradesh- 211004, India
***Corresponding author**- email:* bvasu@mnnit.ac.in, rma1601@mnnit.ac.in
[b]Professor, Department of Mechanical and Aeronautical Engineering, School of Science, Engineering, and Environment (SEE), Newton building, Salford University, Manchester, M54WT, ***UK. E:*** *O.A.Beg@salford.ac.uk* and *A.Kadir@salford.ac.uk*
[C]Professor, Department of Mechanical Engineering, Cleveland State University, Ohio, 44115, ***USA. E:*** *r.gorla@csuohio.edu*

ABSTRACT

This article presents a two-dimensional theoretical study of hemodynamics through a diseased permeable artery with a mild stenosis and an aneurysm present. The effect of metallic nanoparticles on the blood flow is considered, motivated by drug delivery (pharmacology) applications. Two different models are adopted to mimic non-Newtonian characteristics of the blood flow; the Casson (viscoplastic) fluid model is deployed in the core region and the Sisko (viscoelastic) fluid model employed in the peripheral (porous) region. The revised Buongiorno two-component nanofluid model is utilized for nanoscale effects. The blood is considered to contain a homogenous suspension of nanoparticles. The governing equations are derived by extending the Navier-Stokes equations with linear Boussinesq approximation (which simulates both heat and mass transfer). Natural (free) double-diffusive convection is considered to simulate the dual influence of thermal and solutal buoyancy forces. The conservation equations are normalized by employing appropriate non-dimensional variables. The transformed equations are solved numerically using the finite element method with the variational formulation scheme available in the FreeFEM++ code. A comprehensive mesh-independence study is included. The effect of selected parameters (thermophoresis, Brownian motion, Grashof number, thermo-solutal buoyancy ratio, Sisko parameter ratio and permeability parameter) on velocity, temperature, nanoparticle concentration

and hemodynamic pressure have been calculated for two clinically important cases of arteries with a stenosis and an aneurysm. Skin-friction coefficient, Nusselt number, volumetric flow rate and resistance impedance of blood flow are also computed. Colour contours and graphs are employed to visualize the simulated blood flow characteristics. It is observed that by increasing thermal buoyancy parameter i.e. Grashof number (*Gr*), the nanoparticle concentration and temperature decrease whereas velocity increases with an increment in Brownian motion parameter (*Nb*). Furthermore, velocity decreases in the peripheral porous region with elevation in the Sisko material ratio (*m*) and permeability parameter (*k'*). The simulations are relevant to transport phenomena in pharmacology and nano-drug targeted delivery in haematology.

Keywords: *Arterial stenosis, aneurysm, Casson fluid model, Sisko fluid model, Nano-drugs, Porous walls, Thermophoresis, Finite Element Method, FreeFEM++.*

Nomenclature:

D_b	Brownian diffusion coefficient
D_T	Thermophoretic diffusion coefficient
g	Gravitational vector
G_r	Grashof Number
Re	Reynolds Number
Pr	Prandtl Number
S_c	Schmidt Number
$R(z)$	Radius of artery
r	Radial coordinate
z	Axial coordinate
u	Velocity in radial direction
w	Velocity in axial direction
N	Ratio of thermal to buoyancy forces
Nb	Brownian motion parameter
Nt	Thermophoresis parameter
p	Pressure
Q	Volumetric flow rate
λ	Resistance Impedance
Nu	Nusselt Number
C_f	Skin-friction Coefficient
m	Sisko material Parameter
T	Temperature
T_w	Temperature at wall
T_L	Reference temperature

Greek Letters:

μ_1	Asymptotic value of viscosity at very high rate
μ_0	Consistency
κ	Thermal conductivity
ρ_f	Density of the base fluid
ϕ	Nanoparticle volume fraction
μ	Dynamic viscosity
δ	Stenosis depth
ρ_p	Density of the nanoparticles
ϕ_w	Concentration at wall

ϕ_L	Reference mass concentration	τ_c	Yield stress
τ_s	Cauchy stress tensor		

1. INTRODUCTION

Based on the reports of numerous physiological studies, the primary cause of mortality worldwide is due to diseases in the blood vessels and the heart including heart attacks and strokes. According to the data of the World Health Organization (WHO), the percentage of deaths due to non-communicable diseases is 68% from which one-third are attributable to cardiovascular diseases [1]. Cardiovascular disease includes coronary heart disease (CHD), cerebrovascular disease, rheumatic heart disease and numerous other ailments. The cause of these events is the formation of plaque in the lumen, known as *atherosclerosis,* and manifests as a *stenosis* which can grow and block the artery and hence prevent blood supply to the distant body cells. Plaques with calcium in them can also rupture and initiate the formation of blood clotting [2]. Blood is an immensely complex, aqueous polymeric and ionic solution (concentrated suspension) containing several cellular elements and these elements include erythrocytes, leukocytes, and platelets (thrombocytes) in the plasma. Plasma which generally behaves as a Newtonian fluid [3], is composed of water (93%) and electrolytes, organic molecules, numerous proteins (3%), and waste products. The non-Newtonian properties of blood can be seen in the small arteries due to low shear rates. At high shear rate blood usually behaves like a Newtonian fluid as observed in large arteries [4, 5]. A study done by Schmidt- Schonbein *et al.* [6], shows that blood component interaction (e.g. erythrocytes and leukocytes) in the capillaries is the primary cause of non-Newtonian behaviour of blood (biorheology). Through a complex network of arteries, veins, and capillaries, blood flows to the body organs and body cells. The motion of blood is due to continuous pumping by the heart; deoxygenated blood is transported to the heart from the organs through veins and the heart pumps oxygenated blood to the whole body through the arteries. To maintain cell-level metabolism, blood flow ensures the transportation of nutrients, hormones, metabolic wastes, O_2, and CO_2 throughout the body. It regulates the pH, osmotic pressure and temperature of the whole body and protects the body from microbial and mechanical harm [7]. A significant number of studies have been reported by considering blood as a Newtonian fluid. Relevant examples include Bluestein *et al.* [8] and Young and Tsai [9] studied the hydrodynamic characteristics in a healthy blood vessel by considering either laminar or turbulent behaviour of the flow. More recently non-Newtonian hemodynamics has been addressed by a number of investigators. Reddy *et al.* [10]

studied the blood flow by treating the blood as a high impedance couple stress fluid, showing that significant deviation in flow characteristics arise compared with the classical Newtonian model. Several investigators have however analysed theoretically in detail the contribution of blood rheology to coronary artery disease and cerebral aneurysms. Agrawal *et al*. [11] studied the shear-thinning characteristics of blood with a Carreau–Yasuda Model, for coil embolization as a mildly invasive endovascular method for treatment of a cerebral aneurysm. They observed that the blood rheology exerts a prominent role in the performance of the coil which is aimed at reducing fluid loading of the blood vessel and delaying subsequent wall deformation. Priyadharshini and Ponalagusamy [12] used a finite difference computational method to simulate time-dependent magneto-hemodynamics in a tapered arterial stenosis with variable viscosity, considering blood in the core region as viscoelastic Jeffrey fluid and plasma in the peripheral layer as Newtonian. They confirmed that the results with blood rheology included better correlate with experimental data. Arterial blood flow is fundamental to the human circulatory system, and the presence of arterial stenosis adversely influences the health of the cardiovascular system [13]. The essential contributions related to heart diseases (stenosis) via diagnostic tools and simulations of chirurgical treatments such as stents and by-passes, has mobilized strong interest in biologists, medical engineers and scientists in this area [14]. Riahi *et al*. [15] studied the blood flow in an artery containing an overlapping stenosis. Chakravarty *et al*. [16] and Mekheimer and El Kot, [17] each considered hemodynamics in a time-variant tapered stenotic artery. Akbar *et al.* [18] employed the Jeffrey rheological model for blood flow through a tapered artery with a stenosis to study non-Newtonian fluid characteristics. Ellahi *et al.* [19] simulated the arterial blood flow through a mild composite stenosis with Eringen's micropolar model. Razavi *et al.* [20] compared various viscosity models to the Newtonian model for pulsatile hemodynamics in a stenosed carotid artery, noting that with greater degree of stenosis there is increased disturbance induced in the downstream flow of the stenosis and wall shear stress (WSS) which develops at the stenosis throat noticeably. Karimietal [21] implemented the Carreau and modified power-law non-Newtonian models in blood flow via common stenosed carotid arteries and compared the simulation results with the experimental data to highlight the influence of rheology on hemodynamic characteristics.

An *aneurysm* is a balloon-like dilation usually found on the walls of blood arteries including the abdominal artery, cerebral artery, carotid artery, thoracic artery, femoral artery, etc. It develops gradually and grows faster as time passes [22]. The role of hemodynamics in the growth of aneurysms has been the subject of several studies. Mukhopadhyay *et al.* [23] modelled blood flow in an artery featuring a local aneurysm in the presence of haematocrit. Kumar *et al.* [24],

investigated the pulsatile blood flow characteristics using a Saffman particle-fluid suspension two phase model and determined the flow, pressure and shear stress distributions in an artery with an aneurysm. Bluestein *et al.* [25] employed both computational fluid dynamics and digital particle Image Velocimetry (DPIV) to study both laminar and turbulent hemodynamics in an artery with aneurysm and identified the formation of a recirculation zone inside the aneurysm cavity which induces thrombus formation and increases the chances of rupture. As noted above a variety of different non-Newtonian models have been applied to stenotic and aneurysm-modified hemodynamics. An alternative model is the *viscoplastic* Casson fluid model. This model predicts an infinite viscosity at zero shear rate, and a constant viscosity at an infinite rate of shear. It is a robust shear-thinning fluid model and has been explored in several areas of hemodynamics such as blood flow in regular and constricted tubes. Casson [26] initially investigated the validity of this model by studying the flow characteristics of blood observed that at low shear rates, the yield stress for blood is non-zero. Sarifuddin *et al.* [27] presented a mathematical model of blood flow through an asymmetric arterial constriction where the blood is represented as the suspension of erythrocytes in plasma with the Casson fluid model. Blair [28] and Copley [29] established in their studies that for representation of the simple shear behaviour of blood in narrow arteries, the Casson fluid model is arguably the most appropriate since it included a yield stress criterion. Blood is also known to exhibit *viscoelasticity* under certain conditions. A popular and robust model for viscoelasticity in hemodynamics is the Sisko model. It is a relatively simple non-Newtonian model which provides robust predictions for high shear rate flows and is a modification of the power-law model. Originally introduced for lubricants, the Sisko model has been adopted in a number of hemodynamic investigations. Haghighi and Chalak [30] used the Sisko rheological model to simulate blood flow in a stenotic artery with body acceleration effects and a finite difference numerical method. Zaman *et al.* [31] presented a non-linear unsteady blood flow model for a stenosed elastic vessel with the Sisko model. Mekheimer *et al.* [32] developed an unsteady blood flow model for anisotropic elastic tapered arteries with time-variant overlapping stenosis. Ali *et al.* [33] showed that the Sisko fluid model is appropriate for medium and high shear rate scenarios and quite accurately mimics several hemo-rheological characteristics.

An additional feature of real arteries is the permeability of the artery wall. This allows the diffusion of oxygen and other nutrients into the vessel. Several computational studies of hemodynamic flow in permeable arteries have been communicated. Bali and Awasthi [34], and Mishra *et al.* [35], studied the blood flow through a composite stenosis in an artery with a porous wall, although blood was simplified to a Newtonian fluid. Further studies of permeable wall and porosity effects in

blood flow include Jain *et al*. [36] (for stenosed arteries), Tripathi [37] (magnetic blood flow in an inclined artery), Eldesoky [38] (who included slip effects and body acceleration) and Srivastav [39] (for Newtonian blood in a catheterized stenosed artery). The expansion of nanotechnology has revolutionized biomedicine in the 21st century. Many new nanomaterials have also been implemented in a variety of areas in biomechanics and biofluid mechanics. A sub-set of nanomaterials (which include carbon nanotubes, nanoshells, nanorods and nanowires) is nanofluids. Pioneered by Choi and Eastman [40] at Argonne Energy Laboratory in the USA, nanofluids are engineered colloids which are synthesized by suspending metallic or non-metallic nanoparticles in a base fluid. The resulting suspension achieves improved thermal characteristics compared with conventional working fluids in engineering. Although initially developed for automotive and thermal power applications, nanofluids have been successfully utilized in an astonishing range of clinical applications. These have included both theoretical and experimental studies, largely based on the Buongiorno [41] and revised Buongiorno [42,43] model which is a two-component nanoscale formulation or the Tiwari-Das model [44] which is a volume fraction-based doping model (based on the Maxwell-Garnett theory). Improvement in the thermal conductivity of conventional fluids (e.g. water, refrigerant, ethyl glycol and engine oil) has become a prominent area of intensive activity with the objective of enhancing heat transfer characteristics (thermal conductivity, heat transfer coefficient, etc.) and nanoparticles playing an essential role in improving the heat transfer. Buongiorno [41] has presented a comprehensive study of convective transport in nanofluids. Nanofluids display substantial enhancement of thermal conductivity, which is boosted with increasing volumetric fraction of nanoparticles as reported by Masuda *et al.* [45]. Farooq *et al.* [46] and Hayat *et al.* [47] studied stagnation point heat and mass transfer in nanofluid flow over a non-linear stretching sheet. Other heat and mass transfer investigations have considered different nanoparticles and studied temperature and nanoparticle concentration [48]. Thermophoresis and Brownian motion aspects have also been addressed in thermosolutal nanoparticle diffusion from different geometries [49-50]. The classical models are not applicable for the enhancement of thermal conductivity of nanofluids. In recent years, most developed models only include one or two postulated mechanisms of nanofluid thermophysics. For example, there has been a sparsity in fundamental work reported for the determination of the effective thermal diffusivity or heat transfer coefficients for nanofluids in natural convection [51].

Interesting examples of the deployment of nanofluids in medicine include blood purification systems [52], smart bio-nano-polymer coatings for medical devices [53], nano-drug delivery (pharmacological systems) in cardiovascular treatment [54, 55], biodegradable nanoliquids for

cerebral pharmaco-dynamics [56], membrane oxygenator bioreactors [57], orthopaedic lubrication with nano-films (superlubricated poly (3-sulfopropyl methacrylate potassium salt)-grafted mesoporous silica nanoparticles suspended in starch base liquids) [58], pulsed laser ablation (PLA) ultra-pure silicon nanofluid fabrication for cancer therapy [59], smart biomimetic electro-osmotic nanofluid pumps in ocular diagnosis [60], cryopreservation, bone reinforcement via super-paramagnetic nanofluids etc. In hemodynamic therapies, the base liquid is clearly blood and can be doped with a variety of nanoparticles including gold. To prevent in-stent restenosis and to improve the performance of current stents, different nanomaterial coatings, and controlled-release nano-carriers are used [61]. Nano-carriers have the potential for delivery of imaging and diagnostic agents to precisely targeted destinations. Current therapies focus on decreasing the burden of atherosclerotic plaque and stabilizing vulnerable plaques defined as those plaques, which have a tendency to rupture and cause thrombosis [62]. A new type of stent has been designed in recent years and is known as the drug-eluting stent (DES), which reduces the risk of in-stent thrombosis and restenosis caused by bare-metal stents. Different classes with a wide range of drugs have been tested with DES to prevent smooth muscle cell (SMC) growth and proliferation, anti-cancer, and anti-inflammatory agents. Giljohann *et al*. [63], and Kumar *et al*. [64], investigated the effect of gold nanoparticles suspension in blood. Ali *et al.* [65] presented a comprehensive computational model for studied unsteady heat and mass transfer in nanoparticle doped streaming blood flow via a tapered stenotic artery using the Buongiorno model.

A close inspection of the scientific literature has shown that relatively few works have been conducted for hemodynamic transport in porous-walled arteries featuring either a constriction (stenosis) and/or dilation (aneurysm). Furthermore, very little research has appeared considering thermophysical/mass diffusion aspects (e.g. thermo-solutal buoyancy) of obstructed hemodynamics with nanoscale models. Also, the modification in blood pressure distribution in nano-pharmacodynamics has not been extensively studied. Hence the novelty of the present study lies in combining the effect of geometric complexities, non-Newtonian (hemo-rheological behaviour), thermophysics and nanoscale parameters on hemodynamic transport characteristics in obstructed nano-doped blood flow in an artery with porous walls. A mathematical model is developed for steady rheological blood flow, heat transfer and mass (nanoparticle) diffusion in an artery with porous wall featuring both a stenosis and aneurysm (fusiform). The Casson viscoplastic fluid model [66] is deployed in the core part of the artery and a Sisko viscoelastic fluid model [67] is employed in the peripheral region to mimic non-Newtonian characteristics. With appropriate boundary conditions, the non-dimensional transformed conservation equations are solved with the

finite element method using a variational approach based on the FreeFem++ code [68]. Mesh-independence is included. The present simulations are relevant to nano-pharmaco-dynamics and provide a deeper understanding of the complex mechanisms inherent to nano-particle drug treatments for cardiovascular diseases.

2. BIO-RHEOLOGICAL NANO-PHARMACODYNAMIC MODEL

Consider the two-dimensional, laminar, incompressible steady (non-pulsating) hemodynamic flow in an artery with a porous wall. Here the core and peripheral regions are the lumen and porous arterial wall respectively and for convenience the following convention is used throughout the paper - core region (lumen) and peripheral region (porous arterial wall). Blood is simulated as a non-homogeneous fluid with dispersed uniform nanoparticles. Non-Newtonian characteristics are treated with a dual rheological formulation- namely a Casson fluid model in the core region and a Sisko fluid model in the peripheral region. Thermosolutal flow is considered i.e. both heat and mass (nanoparticle) diffusion are incorporated with associated buoyancy effects. A cylindrical coordinate system (r,φ,z) is employed, where r is the radial coordinate, z is axial coordinate and φ is azimuthal coordinate. Axisymmetric flow is studied and therefore contribution in the azimuthal (φ) direction is ignored i.e., the flow is only in the radial (r) and axial (z) direction as depicted in **Fig. (1).** A finite length arterial geometry is studied which contains a sinusoidal-shaped stenosis with a fusiform aneurysm. In the arterial segment, the geometry of the outer layer of the mild stenosis and aneurysm is assumed to be described by:

$$R_1(z)=\begin{cases} -R_p + a\exp\left(-\dfrac{1}{2a^2}(z-\dfrac{l}{2}+0.5)^2\right); & L\le z\le L+L_0 \ (Stenosis) \\ -R_p-(a-0.3)\exp\left(-\dfrac{1}{2a^2}(z-\dfrac{l}{2}+0.5)^2\right); & L+L_2\le z\le L+L_2+L_0 \ (Aneurysm) \\ R_p \quad ; & otherwise \end{cases} \tag{1}$$

The geometry of inner layer of the mild stenosis and aneurysm are simulated with the following Mathematical relations:

$$R(z)=\begin{cases} -R_c + a\exp\left(-\dfrac{1}{2a^2}(z-\dfrac{l}{2}+0.5)^2\right); & L\le z\le L+L_0 \ (Stenosis) \\ -R_c-(a-0.3)\exp\left(-\dfrac{1}{2a^2}(z-\dfrac{l}{2}+0.5)^2\right); & L+L_2\le z\le L+L_2+L_0 \ (Aneurysm) \\ R_c \quad ; & otherwise \end{cases} \tag{2}$$

Here the following notation applies: radius of the artery, radius of the core region of the nonstenotic section and length of the diseased part of the artery are R_p, R_c *and* L_0 respectively. The radius of the inner layer of the artery is taken as $R(z)$ and radius for the outer layer of the artery is taken as $R_1(z)$. The *z*-axis is orientated in the blood flow direction and normal to the *r*- axis. The stenosis is symmetrical and has a maximum height δ with $a = \frac{9}{10}\delta$. **Fig. 1** also visualizes the erythrocytes (red cells) and spherical nanoparticles (drug) suspended in the blood flow in the artery.

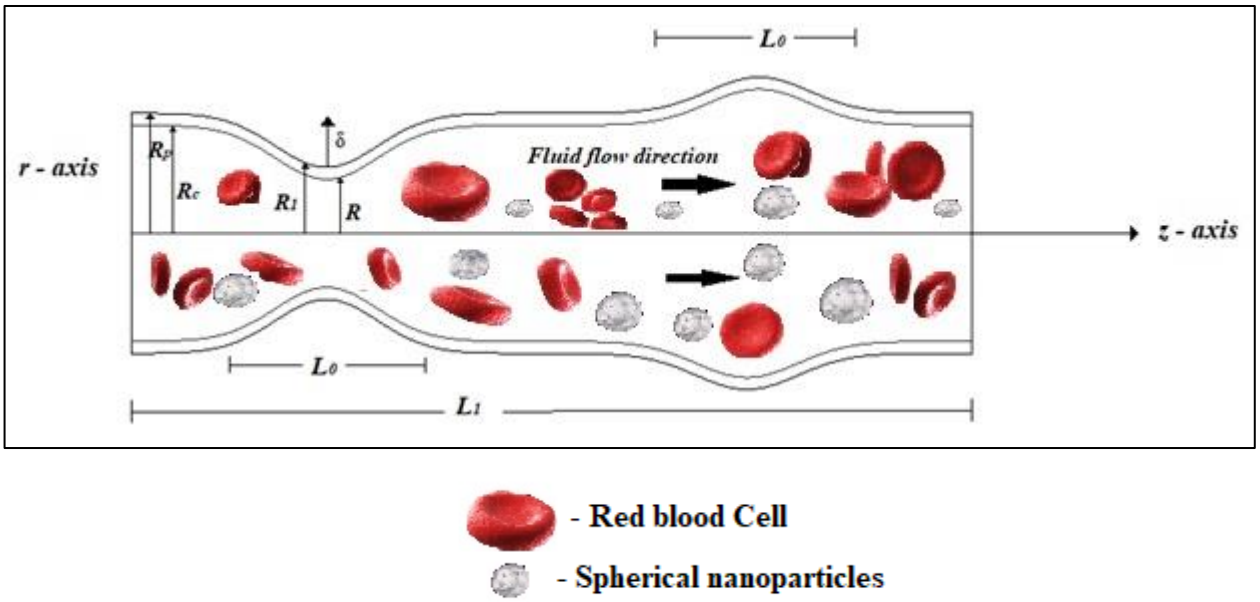

Figure 1. Physical model for biorheological nano-pharmacodynamic flow in an artery with stenosis and aneurysm

For steady axisymmetric flow of blood in the arterial vessel, the velocity vector *V* is assumed to be of the form:

For the core region (Casson fluid model)

$$V_c = [u_c(r,z), 0, w_c(r,z)] \tag{3}$$

For the peripheral (porous) region (Sisko fluid model):

$$V_p = [u_p(r,z), 0, w_p(r,z)] \tag{4}$$

Here u_c, u_p and w_c, w_p are the velocity components in radial and axial directions for both core and porous region. Blood is considered to be an incompressible non-Newtonian fluid (Casson fluid in the core region and Sisko fluid in the peripheral region) containing a homogenous distribution of nano-particles.

Since natural (free) convection is considered, which mobilizes buoyancy forces, the appropriate expression under the Boussinesq's approximation, the nanofluid density is:

$$\rho = \rho_f \left[1 - \beta_T (T - T_L) - \beta_S (\phi - \phi_L)\right] \tag{5}$$

Here ρ_f is the base fluid's density at the reference fluid temperature T_L and reference concentration ϕ_L, β_T *and* β_S are the thermal and solutal expansion coefficients respectively.

The governing equations for conservation of mass, momentum, thermal energy and nanoparticle volume fraction (species) for the nano-pharmacodynamic flow in vectorial form are as follows:

For core region:

$$\nabla \cdot V_c(r,z) = 0 \tag{6}$$

$$\rho_f \left(\frac{\partial V_c}{\partial t} + (V_c \cdot \nabla) V_c \right) = div\, \tau_s + [\rho_f (1 - \beta_T (T - T_L) - \beta_c (\phi - \phi_L))] g \tag{7}$$

$$(\rho c)_p \left(\frac{\partial T}{\partial t} + (V_c \cdot \nabla) T \right) = k \nabla^2 T + (\rho c)_f [D_b (\nabla \phi \cdot \nabla T) + \frac{D_T}{T_L} (\nabla T \cdot \nabla T)] \tag{8}$$

$$\left(\frac{\partial \phi}{\partial t} + (V_c \cdot \nabla) \phi \right) = D_b \nabla^2 \phi + \frac{D_T}{T_L} \nabla^2 T \tag{9}$$

Here ϕ is the nanoparticle volume fraction (e. g. gold).

The constitutive equation for the Cauchy stress tensor in a Casson viscoplastic fluid is given by [66] :

$$\left| \sqrt{\tau_s} \right| = \begin{cases} \left| \sqrt{\tau_c} \right| + \left| \left(\mu \left(\frac{\partial w_c}{\partial r} \right) \right)^{\frac{1}{2}} \right| & when\ \tau > \tau_c \\ \left(\frac{\partial w_c}{\partial r} \right) = 0 \qquad when\, \tau < \tau_c \end{cases} \tag{10}$$

Where τ_c is yield stress and μ is the viscosity of blood.

For peripheral region:

$$\nabla \cdot V_p(r,z) = 0 \tag{11}$$

$$\rho_f \left(\frac{\partial V_p}{\partial t} + (V_p \cdot \nabla) V_p \right) = div\, \tau_s + \frac{\mu V_p}{k'} \tag{12}$$

Where k' is the permeability parameter, and the Cauchy stress tensor for the Sisko fluid is:

$$\tau_s = -pI + S \tag{13}$$

In Eq. (11), due to the restraint of incompressibility, $-pI$ represents the spherical stress and S will be defined as [58]:

$$S = \left(\mu_1 + \mu_0 \left|\sqrt{\dot{\gamma}}\right|^{n-1}\right) A_1 \tag{14}$$

Where n, μ_1, μ_0 are material parameters (which vary for different fluids). The kinematical tensor A_1 can be defined by the following equation

$$A_1 = \nabla V_p + \left(\nabla V_p\right)^t \tag{15}$$

And

$$\dot{\gamma} = \frac{1}{2} tr(A_1)^2 \tag{16}$$

Eqns. (6) - (9) i.e. the *hemodynamic transport equations in the core region* $(\ )_c$ effectively emerge in the following form:

$$\frac{\partial u_c}{\partial r} + \frac{u_c}{r} + \frac{\partial w_c}{\partial z} = 0 \tag{17}$$

$$\rho_f \left[u_c \frac{\partial u_c}{\partial r} + w_c \frac{\partial u_c}{\partial z} \right] = -\frac{\partial p_c}{\partial r} + \frac{1}{r}\frac{\partial}{\partial r}\left(rS_{rr}\right) + \frac{\partial}{\partial z}\left(S_{rz}\right) \tag{18}$$

$$\begin{aligned} \rho_f \left[u_c \frac{\partial w_c}{\partial r} + w_c \frac{\partial w_c}{\partial z} \right] = &-\frac{\partial p_c}{\partial z} + \frac{1}{r}\frac{\partial}{\partial r}\left(rS_{rz}\right) + \frac{\partial}{\partial z}\left(S_{zz}\right) \\ &+ \left(\rho_f (1 - \beta_T (T - T_L) - \beta_S (\phi - \phi_L))\right) g \end{aligned} \tag{19}$$

$$\begin{aligned} (c\rho)_p \left(u_c \frac{\partial T}{\partial r} + w_c \frac{\partial T}{\partial z} \right) = \kappa \left(\frac{\partial^2 T}{\partial r^2} + \frac{1}{r}\frac{\partial T}{\partial r} + \frac{\partial^2 T}{\partial z^2} \right) + (c\rho)_f \left(D_b \left[\frac{\partial \phi}{\partial r}\frac{\partial T}{\partial r} + \frac{\partial \phi}{\partial z}\frac{\partial T}{\partial z} \right] \right. \\ \left. + \frac{D_T}{T_L}\left[\frac{\partial T}{\partial r}\frac{\partial T}{\partial r} + \frac{\partial T}{\partial z}\frac{\partial T}{\partial z} \right] \right) \end{aligned} \tag{20}$$

$$\left(u_c \frac{\partial \phi}{\partial r} + w_c \frac{\partial \phi}{\partial z} \right) = D_b \left(\frac{\partial^2 \phi}{\partial r^2} + \frac{1}{r}\frac{\partial \phi}{\partial r} + \frac{\partial^2 \phi}{\partial z^2} \right) + \frac{D_T}{T_L}\left(\frac{\partial^2 T}{\partial r^2} + \frac{1}{r}\frac{\partial T}{\partial r} + \frac{\partial^2 T}{\partial z^2} \right) \tag{21}$$

The mass and momentum Eqns. *in the peripheral region* $(\ )_p$, assume the form:

$$\frac{\partial u_p}{\partial r} + \frac{u_p}{r} + \frac{\partial w_p}{\partial z} = 0 \tag{22}$$

$$\rho_f \left[u_p \frac{\partial u_p}{\partial r} + w_p \frac{\partial u_p}{\partial z} \right] = -\frac{\partial p_p}{\partial r} + \frac{1}{r}\frac{\partial}{\partial r}\left(rS_{rr}\right) + \frac{\partial}{\partial z}\left(S_{rz}\right) + \frac{\mu}{k'} u_p \tag{23}$$

$$\rho_f \left[u_p \frac{\partial w_p}{\partial r} + w_p \frac{\partial w_p}{\partial z} \right] = -\frac{\partial p_p}{\partial z} + \frac{1}{r}\frac{\partial}{\partial r}\left(rS_{rz}\right) + \frac{\partial}{\partial z}\left(S_{zz}\right) + \frac{\mu}{k'} w_p \tag{24}$$

Here the Cauchy stress tensors are defined as follows:

$$S_{rr} = -2\left[\mu_1 + \mu_0\left\{\left|\left[\left(\frac{\partial u_p}{\partial r}\right)^2 + \left(\frac{u_p}{r}\right)^2 + \left(\frac{\partial w_p}{\partial z}\right)^2 + \left(\frac{\partial w_p}{\partial r} + \frac{\partial u_p}{\partial z}\right)^2\right]^{\frac{1}{2}}\right|^{n-1}\right\}\right]\left(\frac{\partial u_p}{\partial r}\right) \tag{25}$$

$$S_{zz} = -2\left[\mu_1 + \mu_0\left\{\left|\left[\left(\frac{\partial u_p}{\partial r}\right)^2 + \left(\frac{u_p}{r}\right)^2 + \left(\frac{\partial w_p}{\partial z}\right)^2 + \left(\frac{\partial w_p}{\partial r} + \frac{\partial u_p}{\partial z}\right)^2\right]^{\frac{1}{2}}\right|^{n-1}\right\}\right]\left(\frac{\partial w_p}{\partial z}\right) \tag{26}$$

$$S_{rz} = -\left[\mu_1 + \mu_0\left\{\left|\left[\left(\frac{\partial u_p}{\partial r}\right)^2 + \left(\frac{u_p}{r}\right)^2 + \left(\frac{\partial w_p}{\partial z}\right)^2 + \left(\frac{\partial w_p}{\partial r} + \frac{\partial u_p}{\partial z}\right)^2\right]^{\frac{1}{2}}\right|^{n-1}\right\}\right]\left(\frac{\partial w_p}{\partial r} + \frac{\partial u_p}{\partial z}\right) \tag{27}$$

The associated boundary conditions are prescribed as follows:

$$\begin{aligned}
&u_c = u_p = 0,\ w_c = U_0,\ \frac{\partial w_p}{\partial r} = 0,\ \frac{\partial T}{\partial r} = 0,\ \frac{\partial \phi}{\partial r} = 0 \quad at\ r = 0 \\
&w_c = w_p && at\ r = R(z) \\
&w_p = 0 && at\ r = R_1(z)\ (no-slip\ condition) \\
&\frac{D_T}{T_L}\frac{\partial T}{\partial r} + D_b\frac{\partial \phi}{\partial r} = 0 && at\ r = R(z) \\
&T = T_w && at\ r = R(z)
\end{aligned} \tag{28}$$

The wall shear stress at the *inner* and the *outer* wall of the artery are defined as:

$$WSS_{inner} = -\left[\sqrt{\tau_c} + \left(\mu\frac{\partial w_p}{\partial r}\right)^{\frac{1}{2}}\right]^2 \tag{29}$$

$$WSS_{outer} = -\left[\mu_1 + \mu_0\left\{\left|\left[\left(\frac{\partial u_p}{\partial r}\right)^2 + \left(\frac{u_p}{r}\right)^2 + \left(\frac{\partial w_p}{\partial z}\right)^2 + \left(\frac{\partial w_p}{\partial r} + \frac{\partial u_p}{\partial z}\right)^2\right]^{\frac{1}{2}}\right|^{n-1}\right\}\right]\left(\frac{\partial w_p}{\partial r} + \frac{\partial u_p}{\partial z}\right) \tag{30}$$

The heat flux is:

$$q_c = -k\left(\frac{\partial T}{\partial r}\right) \tag{31}$$

Hence the skin friction coefficient and Nusselt number (wall heat transfer rate) are:

$$C_f = \frac{2\tau_w}{\rho_f U_0^{\ 2}} \quad \text{and} \quad Nu = \frac{zq_c}{k\left(T_w - T_L\right)} \tag{32}$$

The volumetric flow rate takes the form:

$$Q = \left[\int_0^{R_c} r w_c dr + \int_{R_c}^{R_p} r w_p dr \right] \tag{33}$$

The flow resistance λ (impedance) will be expressed as:

$$\lambda = \int_0^{L_1} \frac{\left(-\frac{\partial p}{\partial z} \right)}{Q} dz \tag{34}$$

To facilitate a numerical solution of the boundary value problem, it is pertinent to render the derived model as dimensionless. In this spirit, the following non-dimensional variables and parameters are introduced:

$$\begin{aligned}
&\bar{u} = \frac{uL_0}{U_0 \delta},\ \bar{w} = \frac{w}{U_0},\ \bar{z} = \frac{z}{L_0},\ \bar{r} = \frac{r}{R_p},\ \bar{\mu} = \frac{\mu}{\bar{\mu}_0}, \bar{\mu}_0 = \mu_0 \left(\frac{U_0}{R_p} \right)^{n-1}, \bar{\tau} = \frac{R_p}{\mu U_0} \tau \\
&\bar{\theta} = \frac{T - T_L}{T_w - T_L},\ \bar{\phi} = \frac{\phi - \phi_L}{\phi_w - \phi_L}, \bar{p} = \frac{R_p{}^2 p}{U_0 \bar{\mu}_0 L_0}, m = \frac{\mu_1}{\bar{\mu}_0}, \bar{R}(z) = \frac{R(z)}{R_c}, \bar{\lambda} = \frac{\lambda R_p{}^4}{\bar{\mu}_0 L_0}, \tau'_c = \frac{R_p}{\mu U_0} \tau_c \\
&\bar{R}_1(z) = \frac{R_1(z)}{R_p}, \bar{S}_{rr} = \frac{S_{rr} L_0}{U_0 \bar{\mu}_0}, \bar{S}_{zz} = \frac{S_{zz} L_0}{U_0 \bar{\mu}_0}, \bar{S}_{rz} = \frac{S_{rz} R_p}{U_0 \bar{\mu}_0}, r_0 = \frac{R_p}{R_c}, \bar{Q} = \frac{Q}{R_p{}^2 U_0}
\end{aligned} \tag{35}$$

Where $U_0, L_0, R_p, \mu_0, \delta, T_L, T_w, \phi_L$ *and* ϕ_w denote the reference velocity, reference length of the blood vessel, reference radius, reference dynamic viscosity, stenosis depth, reference fluid temperature, vessel wall temperature, reference mass concentration and vessel wall mass concentration in the arterial tube model, respectively. Implementing Eqns. (35) in eqns. (17)-(21) , (22)-(24) and (29)-(34) the following system of dimensionless conservation equations are produced:

For Core region (Casson viscoplastic Fluid):

$$\mathrm{Re}\left[\delta^{*2} \varepsilon^4 \bar{u}_c \frac{\partial \bar{u}_c}{\partial \bar{r}} + \delta^* \varepsilon^4 \bar{w}_c \frac{\partial \bar{u}_c}{\partial \bar{z}} \right] = -\frac{\partial \bar{p}_c}{\partial \bar{r}} + \varepsilon^2 \frac{1}{\bar{r}} \frac{\partial}{\partial \bar{r}} \left(\bar{r} \bar{S}_{rr} \right) + \varepsilon^2 \frac{\partial}{\partial \bar{z}} \left(\bar{S}_{rz} \right) \tag{36}$$

$$\mathrm{Re}\left[\delta^* \varepsilon^2 \bar{u}_c \frac{\partial \bar{w}_c}{\partial \bar{r}} + \varepsilon^2 \bar{w}_c \frac{\partial \bar{w}_c}{\partial \bar{z}} \right] = -\frac{\partial \bar{p}_c}{\partial \bar{z}} + \frac{1}{\bar{r}} \frac{\partial}{\partial \bar{r}} \left(\bar{r} \bar{S}_{rz} \right) + \varepsilon^2 \frac{\partial}{\partial \bar{z}} \left(\bar{S}_{zz} \right) + Gr \left(\bar{\theta} + N \bar{\phi} \right) \tag{37}$$

$$\mathrm{Re}\,\mathrm{Pr}\left(\delta^{*}\varepsilon\bar{u}_c\frac{\partial\bar{\theta}}{\partial\bar{r}}+\varepsilon^{2}\bar{w}_c\frac{\partial\bar{\theta}}{\partial\bar{z}}\right)=\left(\frac{\partial^{2}\bar{\theta}}{\partial\bar{r}^{2}}+\frac{1}{\bar{r}}\frac{\partial\bar{\theta}}{\partial\bar{r}}+\varepsilon^{2}\frac{\partial^{2}\bar{\theta}}{\partial\bar{z}^{2}}\right)+N_b\left[\frac{\partial\bar{\phi}}{\partial\bar{r}}\frac{\partial\bar{\theta}}{\partial\bar{r}}+\varepsilon^{2}\frac{\partial\bar{\phi}}{\partial\bar{z}}\frac{\partial\bar{\theta}}{\partial\bar{z}}\right]+N_t\left[\frac{\partial\bar{\theta}}{\partial\bar{r}}\frac{\partial\bar{\theta}}{\partial\bar{r}}+\varepsilon^{2}\frac{\partial\bar{\theta}}{\partial\bar{z}}\frac{\partial\bar{\theta}}{\partial\bar{z}}\right] \tag{38}$$

$$\mathrm{Re}\,Sc\left(\delta^{*}\varepsilon\bar{u}_c\frac{\partial\bar{\phi}}{\partial\bar{r}}+\varepsilon\bar{w}_c\frac{\partial\bar{\phi}}{\partial\bar{z}}\right)=\left(\frac{\partial^{2}\bar{\phi}}{\partial\bar{r}^{2}}+\frac{1}{\bar{r}}\frac{\partial\bar{\phi}}{\partial\bar{r}}+\varepsilon^{2}\frac{\partial^{2}\bar{\phi}}{\partial\bar{z}^{2}}\right)+\frac{Nt}{Nb}\left(\frac{\partial^{2}\bar{\theta}}{\partial\bar{r}^{2}}+\frac{1}{\bar{r}}\frac{\partial\bar{\theta}}{\partial\bar{r}}+\varepsilon^{2}\frac{\partial^{2}\bar{\theta}}{\partial\bar{z}^{2}}\right) \tag{39}$$

The Cauchy stress tensor for the Casson fluid in non-dimensional form becomes:

$$\sqrt{\bar{\tau}}=\sqrt{\tau_c'}+\left(\left(\frac{\partial\bar{w}_c}{\partial\bar{r}}\right)\right)^{\frac{1}{2}} \tag{40}$$

For the Peripheral region (Sisko viscoplastic fluid):

$$\mathrm{Re}\left[\delta^{*2}\varepsilon^{4}\bar{u}_p\frac{\partial\bar{u}_p}{\partial\bar{r}}+\delta^{*}\varepsilon^{4}\bar{w}_p\frac{\partial\bar{u}_p}{\partial\bar{z}}\right]=-\frac{\partial\bar{p}_p}{\partial\bar{r}}+\varepsilon^{2}\frac{1}{\bar{r}}\frac{\partial}{\partial\bar{r}}\left(\bar{r}\bar{S}_{rr}\right)+\varepsilon^{2}\frac{\partial}{\partial\bar{z}}\left(\bar{S}_{rz}\right)+\delta^{*}\varepsilon^{2}\frac{{R_p}^{2}\bar{\mu}}{k'}\bar{u}_p \tag{41}$$

$$\mathrm{Re}\left[\delta^{*}\varepsilon^{2}\bar{u}_p\frac{\partial\bar{w}_p}{\partial\bar{r}}+\varepsilon^{2}\bar{w}_p\frac{\partial\bar{w}_p}{\partial\bar{z}}\right]=-\frac{\partial\bar{p}_p}{\partial\bar{z}}+\frac{1}{\bar{r}}\frac{\partial}{\partial\bar{r}}\left(\bar{r}\bar{S}_{rz}\right)+\varepsilon^{2}\frac{\partial}{\partial\bar{z}}\left(\bar{S}_{zz}\right)+\frac{{R_p}^{2}\bar{\mu}}{k'}\bar{w}_p \tag{42}$$

The Cauchy stress tensors i.e. eqns. (25)-(27) in dimensionless form become:

$$\bar{S}_{rr}=-2\left[m+\left\{\left|\left[\left(\delta^{*}\varepsilon\frac{\partial\bar{u}_p}{\partial\bar{r}}\right)^{2}+\left(\delta^{*}\varepsilon\frac{\bar{u}_p}{\bar{r}}\right)^{2}+\left(\varepsilon\frac{\partial\bar{w}_p}{\partial\bar{z}}\right)^{2}+\left(\frac{\partial\bar{w}_p}{\partial\bar{r}}+\delta^{*}\varepsilon^{2}\frac{\partial\bar{u}_p}{\partial\bar{z}}\right)^{2}\right]^{\frac{1}{2}}\right|^{n-1}\right\}\right]\left(\delta^{*}\frac{\partial\bar{u}_p}{\partial\bar{r}}\right) \tag{43}$$

$$\bar{S}_{zz}=-2\left[m+\left\{\left|\left[\left(\delta^{*}\varepsilon\frac{\partial\bar{u}_p}{\partial\bar{r}}\right)^{2}+\left(\delta^{*}\varepsilon\frac{\bar{u}_p}{\bar{r}}\right)^{2}+\left(\varepsilon\frac{\partial\bar{w}_p}{\partial\bar{z}}\right)^{2}+\left(\frac{\partial\bar{w}_p}{\partial\bar{r}}+\delta^{*}\varepsilon^{2}\frac{\partial\bar{u}_p}{\partial\bar{z}}\right)^{2}\right]^{\frac{1}{2}}\right|^{n-1}\right\}\right]\left(\frac{\partial\bar{w}_p}{\partial\bar{z}}\right) \tag{44}$$

$$\bar{S}_{rz}=-\left[m+\left\{\left|\left[\left(\delta^{*}\varepsilon\frac{\partial\bar{u}_p}{\partial\bar{r}}\right)^{2}+\left(\delta^{*}\varepsilon\frac{\bar{u}_p}{\bar{r}}\right)^{2}+\left(\varepsilon\frac{\partial\bar{w}_p}{\partial\bar{z}}\right)^{2}+\left(\frac{\partial\bar{w}_p}{\partial\bar{r}}+\delta^{*}\varepsilon^{2}\frac{\partial\bar{u}_p}{\partial\bar{z}}\right)^{2}\right]^{\frac{1}{2}}\right|^{n-1}\right\}\right]\left(\frac{\partial\bar{w}_p}{\partial\bar{r}}+\delta^{*}\varepsilon^{2}\frac{\partial\bar{u}_p}{\partial\bar{z}}\right) \tag{45}$$

Hemodynamic simulations are to be explored for the case of a mild stenotic artery. The nondimensional geometric parameters featured in the preceding terms defined above are stenosis height parameter ($\delta^{*}=\delta/R_p$ <<1) and the vessel aspect ratio ($\varepsilon=R_p/L_0$). For the subsequent analysis, we shall assume that δ^{*} << 1 and ε = O (1), i.e., the maximum height of the stenosis is small in comparison with the radius of the artery and also that the radius of the artery and length of

the stenotic region are of comparable magnitude [69]. After applying the above assumptions in the normalized system of Eqns. (36) – (39), we obtain for *the core region (Casson viscoplastic fluid):*

$$\frac{\partial \overline{p}_c}{\partial \overline{r}} = 0 \tag{46}$$

$$\frac{\partial \overline{p}_c}{\partial \overline{z}} = \frac{1}{\overline{r}}\tau_c' + \frac{1}{\overline{r}}\frac{\partial \overline{w}_c}{\partial \overline{r}} + \sqrt{\tau_c'}\left(\frac{\partial \overline{w}_c}{\partial \overline{r}}\right)^{\frac{1}{2}}\left(\frac{2}{\overline{r}} + \left(\frac{\partial \overline{w}_c}{\partial \overline{r}}\right)\frac{\partial^2 \overline{w}_c}{\partial \overline{r}^2}\right) + \left(\frac{\partial^2 \overline{w}_c}{\partial \overline{r}^2}\right) + Gr\left(\overline{\theta} + N\overline{\phi}\right) \tag{47}$$

$$\left(\frac{\partial^2 \overline{\theta}}{\partial \overline{r}^2} + \frac{1}{\overline{r}}\frac{\partial \overline{\theta}}{\partial \overline{r}}\right) + \left(Nb\left[\frac{\partial \overline{\phi}}{\partial \overline{r}}\frac{\partial \overline{\theta}}{\partial \overline{r}}\right] + Nt\left[\frac{\partial \overline{\theta}}{\partial \overline{r}}\frac{\partial \overline{\theta}}{\partial \overline{r}}\right]\right) = 0 \tag{48}$$

$$\left(\frac{\partial^2 \overline{\phi}}{\partial \overline{r}^2} + \frac{1}{\overline{r}}\frac{\partial \overline{\phi}}{\partial \overline{r}}\right) + \frac{Nt}{Nb}\left(\frac{\partial^2 \overline{\theta}}{\partial \overline{r}^2} + \frac{1}{\overline{r}}\frac{\partial \overline{\theta}}{\partial \overline{r}}\right) = 0 \tag{49}$$

After applying the above assumptions in the normalized system of Eqns. (41) – (45), we get for the *peripheral region (Sisko viscoelastic fluid)*:

$$\frac{\partial \overline{p}_p}{\partial \overline{r}} = 0 \tag{50}$$

$$\frac{\partial \overline{p}_p}{\partial \overline{z}} = \left(\frac{1}{\overline{r}}\frac{\partial \overline{w}_p}{\partial \overline{r}} + \frac{\partial^2 \overline{w}_p}{\partial \overline{r}^2}\right)\left(m + \left(\frac{\partial \overline{w}_p}{\partial \overline{r}}\right)^{n-1}\right) + \frac{\partial^2 \overline{w}_p}{\partial \overline{r}^2}\left((n-1)\left(\frac{\partial \overline{w}_p}{\partial \overline{r}}\right)^{n-2}\right)\frac{\partial \overline{w}_p}{\partial \overline{r}} + \overline{\mu}^* \overline{w}_p \tag{51}$$

The associated non-dimensional boundary conditions emerges as:

$$\begin{aligned}
&\overline{u}_c = \overline{u}_p = 0,\ \overline{w}_c = 1,\ \frac{\partial \overline{w}_p}{\partial \overline{r}} = 0,\ \frac{\partial \overline{\theta}}{\partial \overline{r}} = 0,\ \frac{\partial \overline{\phi}}{\partial \overline{r}} = 0 \quad at\ \overline{r} = 0 \\
&\overline{w}_c = \overline{w}_p \qquad\qquad at\ \overline{r} = r_0\overline{R}(z) \\
&\overline{w}_p = 0 \qquad\qquad at\ \overline{r} = \overline{R}_1(z) \\
&N_t\frac{\partial \overline{\theta}}{\partial \overline{r}} + N_b\frac{\partial \overline{\phi}}{\partial \overline{r}} = 0 \qquad\qquad at\ \overline{r} = r_0\overline{R}(z) \\
&\overline{\theta} = 1 \qquad\qquad at\ \overline{r} = r_0\overline{R}(z)
\end{aligned} \tag{52}$$

After non-dimensionalization of the skin friction coefficient and Nusselt number, the following expressions are obtained:

Skin friction coefficient at the inner wall:

$$\frac{1}{2}C_f'\,\mathrm{Re} = -\left[\sqrt{\tau_c'} + \left(\overline{\mu}\frac{\partial \overline{w}_p}{\partial \overline{r}}\right)^{\frac{1}{2}}\right]^2 \tag{53}$$

Skin friction coefficient at the outer wall:

$$\frac{1}{2}C_f' \,\mathrm{Re} = -\left[m + \left(\frac{\partial \overline{w}_p}{\partial \overline{r}} \right)^{n-1} \right] \left(\frac{\partial \overline{w}_p}{\partial \overline{r}} \right) \tag{54}$$

Nusselt number at any wall:

$$Nu' \,\mathrm{Re} = -\overline{z} \left(\frac{\partial \overline{\theta}}{\partial \overline{r}} \right) \tag{55}$$

Volumetric flow rate:

$$\overline{Q} = \int_0^{R_c} \overline{r}\,\overline{w}_c d\overline{r} + \int_{R_c}^{R_p} \overline{r}\,\overline{w}_p d\overline{r} \tag{56}$$

Hemodynamic resistance (impedance):

$$\overline{\lambda} = \int_0^{L_1} \frac{\left(-\frac{\partial \overline{p}}{\partial \overline{z}} \right)}{\overline{Q}} d\overline{z} \tag{57}$$

In Eqns. (46)-(57) the Brownian motion parameter, $Nb = \frac{D_b(\phi_w - \phi_L)(\rho c)_f}{\kappa}$, thermophoresis parameter $Nt = \frac{D_T(T_w - T_L)(\rho c)_f}{T_L \kappa}$, the Grashof number $Gr = \frac{(T_w - T_L)\rho_{f,w} g R_p{}^2 \beta_T}{U_0 \overline{\mu}_0}$, the solutal to thermal buoyancy ratio $N = \frac{\beta_S(\phi_w - \phi_L)}{\beta_T(T_w - T_L)}$, the Reynolds number $\mathrm{Re} = \frac{\rho_f U_0 L_0}{\overline{\mu}_0}$, Prandtl number $\mathrm{Pr} = \frac{c_p \overline{\mu}_0}{k}$, and Schmidt number $S_c = \frac{\overline{\mu}_0}{\rho_f D_b}$, peripheral viscosity $\overline{\mu}^* = \frac{\overline{\mu} R^2{}_p}{k'}$, and also $C_f{}' = C_f \left(\frac{U_0}{L_0} \right)$, $Nu' = Nu \frac{\overline{\mu}_0 R_p}{\rho_f U_o}$

3. NUMERICAL COMPUTATIONS WITH FreeFEM++ CODE

The non-dimensional boundary value problem derived i.e. Eqns. (46)-(51) with boundary conditions (52) is still quite formidable owing to strong nonlinearity, coupling of different variables and two space variables. A powerful computational scheme is therefore essential to obtain fast and rapidly convergent solutions. Here the finite element method (FEM) with the variational approach as available in the FreeFEM++ software is selected. The finite element method is the most versatile numerical method both for accommodating complex geometries and also material nonlinearity, two key features of the current nano-pharmacodynamic biorheological

problem under investigation. Discretization of the flow domain is central to finite element simulation and involves division of domain of the problem into multiple subdomains. A set of element equations represents each subdomain. In the final solution, re-assembly of all sets of element equations into a global system of equations is executed systematically in the finite element code. Extensive details of the mathematical and algorithmic foundations of FREEFEM++ are given by Hecht [68]. The impressive versatility of FEM in engineering mechanics and multi-physics is provided in the treatise of Bathe [70]. Some other applications of FEM in hemodynamics (e.g. biomagnetics, pulsatile flows, tissue diffusion etc) have been reviewed by Bég [71]. FREEFEM++ has been employed successfully and very recently in simulating cardiovascular stenotic flows by Dubey and Vasu [72]. Here we provide extensive details of the finite element formulation employed via FREEFEM++ in solving the problem at hand. A weak formulation of the partial differential equation system (46)-(51) is derived by first defining the function spaces:

$$\begin{aligned} X &= \left\{ \bar{u} \in \left(H_1(\Omega) \right) \middle| \bar{u} = a \ on \ \Gamma_{in}, \bar{u} = 0 \ on \ \Gamma_{wall} \right\} \\ Q &= \left\{ \bar{u} \in \left(H_1(\Omega) \right) \middle| \bar{u} = 0 \ on \ \Gamma_{in} \cup \Gamma_{wall} \right\} \end{aligned} \tag{58}$$

The weak form of Eqns. (46) - (51) is obtained by determining w ∈ X and ϕ, θ ∈ P such that every $u_1, u_2 \in Q$ and p_1, p_2, v, $q \in P$ where $P = L^2(\Omega)$. Therefore, the weak formulation of Eqns. (46) – (51) will emerges as:

For the Core Region (Casson fluid):

$$\int_{\Omega} \frac{\partial \bar{p}_c}{\partial \bar{r}} \cdot p_1 \ d\bar{r} = 0 \tag{59}$$

$$\begin{aligned} &\int_{\Omega} \frac{\partial \bar{p}_c}{\partial \bar{z}} \cdot p_1 \ d\bar{r} - \int_{\Omega} \frac{1}{\bar{r}} \tau_c' \cdot u_1 \ d\bar{r} - \int_{\Omega} \frac{1}{\bar{r}} \frac{\partial \bar{w}_c}{\partial \bar{r}} \cdot u_1 \ d\bar{r} - \int_{\Omega} \left(\frac{2}{\bar{r}} + \frac{\partial \bar{w}_c}{\partial \bar{r}} \frac{\partial^2 \bar{w}_c}{\partial \bar{r}^2} \right) \sqrt{\tau_c'} \left(\frac{\partial \bar{w}_c}{\partial \bar{r}} \right)^{\frac{1}{2}} \cdot u_1 \ d\bar{r} \\ &- \int_{\Omega} \left(\frac{\partial^2 \bar{w}_c}{\partial \bar{r}^2} \right) \cdot u_1 \, d\bar{r} \ - \int_{\Omega} Gr \bar{\theta} \cdot u_1 \ d\bar{r} - \int_{\Omega} Gr \, N \bar{\phi} \cdot u_1 \ d\bar{r} = 0 \end{aligned} \tag{60}$$

$$\int_{\Omega} \frac{\partial^2 \bar{\theta}}{\partial \bar{r}^2} \cdot v \ d\bar{r} + \int_{\Omega} \frac{1}{\bar{r}} \frac{\partial \bar{\theta}}{\partial \bar{r}} \cdot v \ d\bar{r} + \int_{\Omega} Nb \left[\frac{\partial \bar{\phi}}{\partial \bar{r}} \frac{\partial \bar{\theta}}{\partial \bar{r}} \right] \cdot v \ d\bar{r} + \int_{\Omega} Nt \left[\frac{\partial \bar{\theta}}{\partial \bar{r}} \frac{\partial \bar{\theta}}{\partial \bar{r}} \right] \cdot v \ d\bar{r} = 0 \tag{61}$$

$$\int_{\Omega} \frac{\partial^2 \bar{\phi}}{\partial \bar{r}^2} \cdot q \ d\bar{r} + \int_{\Omega} \frac{1}{\bar{r}} \frac{\partial \bar{\phi}}{\partial \bar{r}} \cdot q \ d\bar{r} + \int_{\Omega} \frac{Nt}{Nb} \left(\frac{\partial^2 \bar{\theta}}{\partial \bar{r}^2} + \frac{1}{\bar{r}} \frac{\partial \bar{\theta}}{\partial \bar{r}} \right) \cdot q \ d\bar{r} = 0 \tag{62}$$

For the Peripheral region (Sisko fluid):

$$\int_{\Omega} \frac{\partial \overline{p}_p}{\partial \overline{r}} \cdot p_2 \; d\overline{r} = 0 \tag{63}$$

$$\begin{aligned} &\int_{\Omega} \frac{\partial \overline{p}_p}{\partial \overline{z}} \cdot p_2 \; d\overline{r} - \int_{\Omega} \left(\frac{1}{\overline{r}} \frac{\partial \overline{w}_p}{\partial \overline{r}} + \frac{\partial^2 \overline{w}_p}{\partial \overline{r}^2} \right) \left(m + \left(\frac{\partial \overline{w}_p}{\partial \overline{r}} \right)^{n-1} \right) \cdot u_2 \; d\overline{r} \\ &\quad - \int_{\Omega} \frac{\partial^2 \overline{w}_p}{\partial \overline{r}^2} \left((n-1) \left(\frac{\partial \overline{w}_p}{\partial \overline{r}} \right)^{n-2} \right) \frac{\partial \overline{w}_p}{\partial \overline{r}} \cdot u_2 \; d\overline{r} - \int_{\Omega} \overline{\mu}^* \overline{w}_p \cdot u_2 \; d\overline{r} = 0 \end{aligned} \tag{64}$$

To attain the requisite smoothness of the solutions which is bounded due to the weaker restriction, these differential equations cannot be solved directly. Therefore, the finite dimensional subspaces have to be defined as $Q_h \subset Q$ and $P_h \subset P$. Consider the finite dimensional approximations as $u_{1h}, u_{2h} \subset Q_h$ and $p_{1h}, p_{2h}, v_h, q_h \subset P_h$. In view of the finite dimensional approximation, the set of Eqns. (59)-(64) becomes:

For the Core Region (Casson fluid):

$$\int_{\Omega} \frac{\partial \overline{p}_c}{\partial \overline{r}} \cdot p_{1h} \, d\overline{r} = 0 \tag{65}$$

$$\begin{aligned} &\int_{\Omega} \frac{\partial \overline{p}_c}{\partial \overline{z}} \cdot p_{1h} \, d\overline{r} - \int_{\Omega} \frac{1}{\overline{r}} \tau_c' \cdot u_{1h} \; d\overline{r} - \int_{\Omega} \frac{1}{\overline{r}} \frac{\partial \overline{w}_c}{\partial \overline{r}} \cdot u_{1h} \; d\overline{r} - \int_{\Omega} \left(\frac{2}{\overline{r}} + \frac{\partial \overline{w}_c}{\partial \overline{r}} \frac{\partial^2 \overline{w}_c}{\partial \overline{r}^2} \right) \sqrt{\tau_c'} \left(\frac{\partial \overline{w}_c}{\partial \overline{r}} \right)^{\frac{1}{2}} \cdot u_{1h} \; d\overline{r} \\ &\quad - \int_{\Omega} \left(\frac{\partial^2 \overline{w}_c}{\partial \overline{r}^2} \right) \cdot u_{1h} \, d\overline{r} \; - \int_{\Omega} Gr \overline{\theta} \cdot u_{1h} \; d\overline{r} - \int_{\Omega} Gr \, N \overline{\phi} \cdot u_{1h} \; d\overline{r} = 0 \end{aligned} \tag{66}$$

$$\int_{\Omega} \frac{\partial^2 \overline{\theta}}{\partial \overline{r}^2} \cdot v_h \; d\overline{r} + \int_{\Omega} \frac{1}{\overline{r}} \frac{\partial \overline{\theta}}{\partial \overline{r}} \cdot v_h \; d\overline{r} + \int_{\Omega} Nb \left[\frac{\partial \overline{\phi}}{\partial \overline{r}} \frac{\partial \overline{\theta}}{\partial \overline{r}} \right] \cdot v_h \; d\overline{r} + \int_{\Omega} Nt \left[\frac{\partial \overline{\theta}}{\partial \overline{r}} \frac{\partial \overline{\theta}}{\partial \overline{r}} \right] \cdot v_h \; d\overline{r} = 0 \tag{67}$$

$$\int_{\Omega} \frac{\partial^2 \overline{\phi}}{\partial \overline{r}^2} \cdot q_h \, d\overline{r} + \int_{\Omega} \frac{1}{\overline{r}} \frac{\partial \overline{\phi}}{\partial \overline{r}} \cdot q_h \; d\overline{r} + \int_{\Omega} \frac{Nt}{Nb} \left(\frac{\partial^2 \overline{\theta}}{\partial \overline{r}^2} + \frac{1}{\overline{r}} \frac{\partial \overline{\theta}}{\partial \overline{r}} \right) \cdot q_h \; d\overline{r} = 0 \tag{68}$$

For the Peripheral region (Sisko fluid):

$$\int_{\Omega} \frac{\partial \overline{p}_p}{\partial \overline{r}} \cdot p_{2h} \; d\overline{r} = 0 \tag{69}$$

$$\int_{\Omega} \frac{\partial \overline{p}_p}{\partial \overline{z}} \cdot p_{2h}\, d\overline{r} - \int_{\Omega} \left(\frac{1}{\overline{r}} \frac{\partial \overline{w}_p}{\partial \overline{r}} + \frac{\partial^2 \overline{w}_p}{\partial \overline{r}^2} \right) \left(m + \left(\frac{\partial \overline{w}_p}{\partial \overline{r}} \right)^{n-1} \right) \cdot u_{2h}\, d\overline{r}$$
$$- \int_{\Omega} \frac{\partial^2 \overline{w}_p}{\partial \overline{r}^2} \left((n-1) \left(\frac{\partial \overline{w}_p}{\partial \overline{r}} \right)^{n-2} \right) \frac{\partial \overline{w}_p}{\partial \overline{r}} \cdot u_{2h}\, d\overline{r} - \int_{\Omega} \overline{\mu}^* \overline{w}_p \cdot u_{2h}\, d\overline{r} = 0 \tag{70}$$

The transformed equations (65)-(70) with boundary conditions (52) are solved numerically using finite element method through the variational formulation scheme with FreeFEM++ [68, 72]. An unstructured fixed mesh (grid) comprising **111,662** piecewise linear triangular elements with bubble (P1*b*) and **168,194** nodes, is implemented for the discretization of the arterial flow domain, and depicted in Figure 2. The mesh is constructed by utilizing the automatic FreeFEM++ mesh generator which is based on the popular Delaunay-Voronoi algorithm. The non-linear system of governing equations is solved by employing the **G**eneralized **M**inimal **Res**idual (GMRES) iteration method. In the fixed mesh, a minimum step size ($h_{\min}$), 0.0132355 is considered with the tolerance of computation $< 10^{-6}$ for all the numerical experiments.

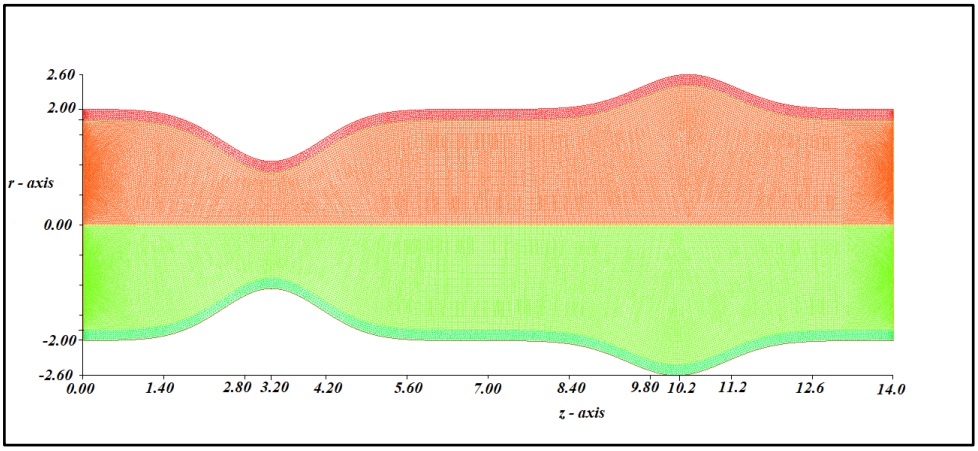

Figure 2. Unstructured fixed mesh of triangular elements

4. MESH INDEPENDENCE ANALYSIS

By conducting several different finite element mesh (grid) distribution tests, it may be established whether the calculated numerical results are grid-independent or not. The numerical values for skin-friction coefficients, at the stenosis and aneurysm, for various designs comprising unstructured fixed mesh elements with vertices and triangular elements, are provided in **Figure 3**. Eight different mesh distributions have been tested to ensure the simulated numerical results are mesh independent. Therefore, the selected mesh for the present calculations consisted of 111662 triangular elements and 168194 nodes, respectively. From Table 1 and figure 2, it is evident that

increasing the mesh element density beyond this design does not modify the numerical values for non-dimensional skin-friction coefficient significantly in the domain with the parametric values prescribed i.e. ***m = 0.657, Nb = 0.6, Nt = 0.6, Gr = 1.0, N = 0.2*** at ***r = 1.095, z = 3.20*** and ***r = 2.60, z = 10.80*** respectively. Mesh independent results are therefore ensured with the mesh design comprising 168194 nodes and 111662 triangular elements (simulation number 6 in **Table 1**).

Table 1. Grid Independency analysis with ***m = 0.657, Nb = 0.6, Nt = 0.6, Gr = 1.0, N = 0.2*** at ***r = 1.095, z = 3.20*** and ***r = 2.60, z = 10.80***

S. No.	Number of Elements	Number of Nodes	Skin-friction coeff. (Stenosis)	Skin-friction coeff. (Aneurysm)
1.	4260	6521	1.3686	1.7108
2.	10016	15245	1.5318	1.7232
3.	25324	38287	1.688	1.9791
4.	58488	88233	1.7003	2.5505
5.	98774	148762	1.7501	2.5788
6.	**111662**	**168194**	**1.7751**	**2.6251**
7.	150038	225758	1.7758	2.6627
8.	161558	243138	1.7921	2.6637

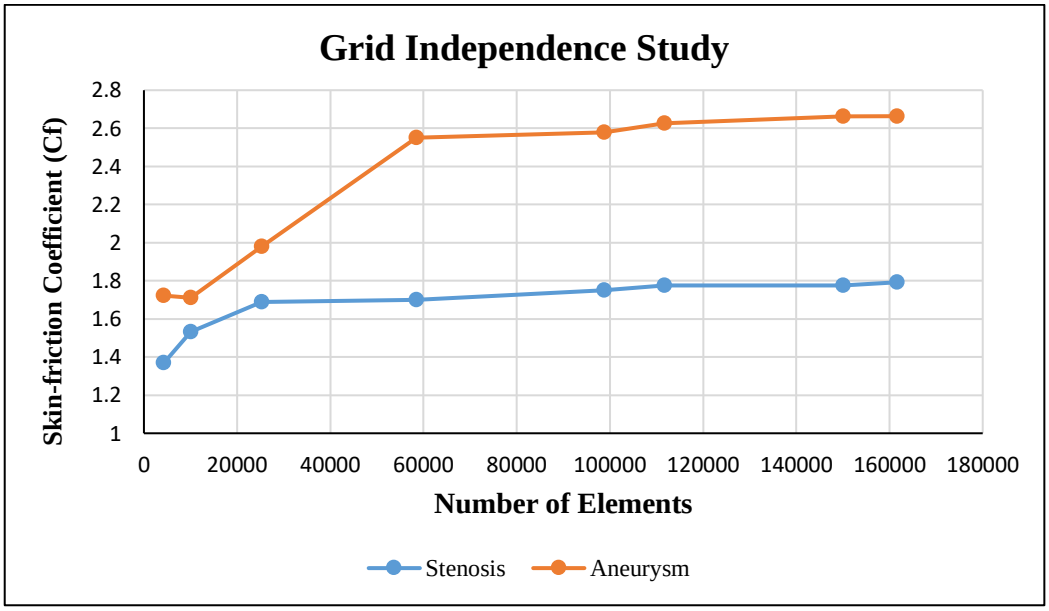

Figure 3: Grid Independence study (Skin friction coefficient)

5. RESULTS AND DISCUSSION

An extensive investigation of the impact of the key multi-physical parameters such as Sisko rheological material parameter ratio (m), permeability parameter ($k^{'}$), on the velocity in porous (peripheral) region and also the influence of Grashof number (Gr), thermophoresis parameter (Nt),

Brownian motion parameter (N_b) and solutal to thermal buoyancy ratio (N) the principal hemodynamic transport characteristics i.e. velocity, temperature and nanoparticle concentration is presented graphically as contour plots in the core and peripheral (porous) regions in **Figs. 4-31**. Numerical results are also given in **Tables 4-10**. Further, the effects of various parameters on physiological flow properties such as the local skin friction coefficient ($\frac{1}{2}\mathrm{Re}\,C_f^*$), Nusselt number ($Nu'\,\mathrm{Re}$), Volumetric flow rate (Q) and hemodynamic resistance are also addressed. For FREEFEM++ computations, the default values of various parameters are considered as **Table 2**.

Table 2: Data employed in FREEFEM++ computations (unless otherwise indicated)

Parameter	***n***	***M***	***Gr***	μ^*	L_1	L_0	***N***	***Nb***	***Nt***	τ_c'	***l***
Values	1.4	0.657	1.0	2.4	14.0	3.20	0.2	0.3	0.3	0.3	7.0

Table 3: Comparison of temperature (θ) values, using the present scheme with the existing results for fixed values of *Nb = 0.3, Nt = 0.3, Gr = 1.0.*

Symmetric Stenosis			
r - axis	**Analytical values of temperature (θ) given by Ellahi et al. [73]**	**Values of temperature (θ) by implementation of FEM on Ellahi et al. [73] modelled problem**	**Values of temperature (θ) in the present study using FEM**
0.05	0.015202	0.015207	0.015207
0.25	0.014947	0.014688	0.014688
0.45	0.013755	0.013169	0.013169
0.55	0.012600	0.012583	0.012583
0.6	0.011851	0.011661	0.011661
0.65	0.010977	0.010132	0.010132
0.75	0.008812	0.008612	0.008612
0.8	0.007495	0.007093	0.007093
0.85	0.005995	0.005576	0.005576
0.9	0.004281	0.004055	0.004055
1.0	0.0	0.0	0.0

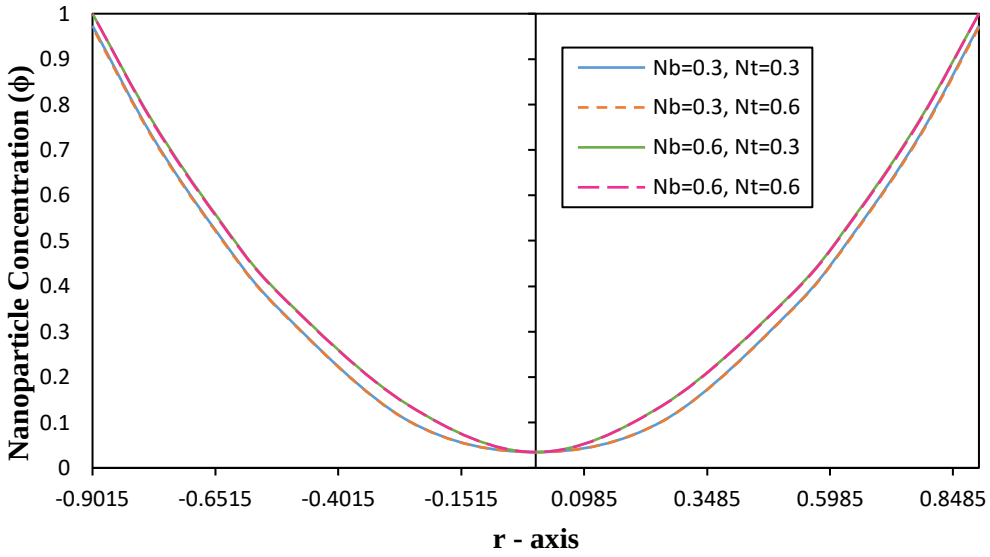

Figure 4 Effect of ***Nb*** and ***Nt*** on nanoparticle concentration in at stenosis in the core region when ***z*** *= 3.20, Gr=1.0, N=0.5*

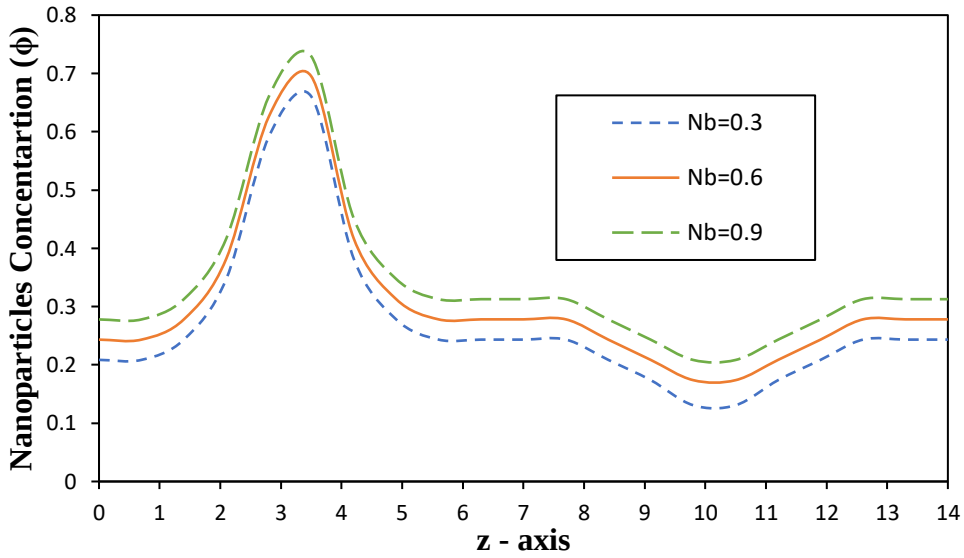

Figure 5 Effect of ***Nb*** on nanoparticles concentration in core region for *r=0.78, Gr=1.0 Nt =0.3 and N=0.5*

Table 4: Nanoparticles concentration for *Gr = 1.0 and N = 0.5,* at stenosis in core region

r - axis	*Nb = 0.3* *Nt = 0.3*	*Nb = 0.3* *Nt = 0.6*	*Nb = 0.6* *Nt = 0.3*	*Nb = 0.6* *Nt = 0.6*	*Nb = 0.9* *Nt = 0.3*	*Nb = 0.9* *Nt = 0.6*
0.0	0.034777	0.034644	0.034762	0.034635	0.034745	0.034619
0.13	0.069538	0.069287	0.069524	0.06927	0.069491	0.069237
0.26	0.10431	0.10393	0.13905	0.13854	0.17373	0.17309
0.39	0.20861	0.20786	0.24334	0.24245	0.27796	0.27695
0.52	0.34769	0.34644	0.38238	0.38099	0.41694	0.41542
0.65	0.52153	0.51965	0.55619	0.55416	0.59067	0.58852
0.78	0.73015	0.72751	0.76447	0.76197	0.79925	0.79623
0.9015	1	1	1	1	1	1

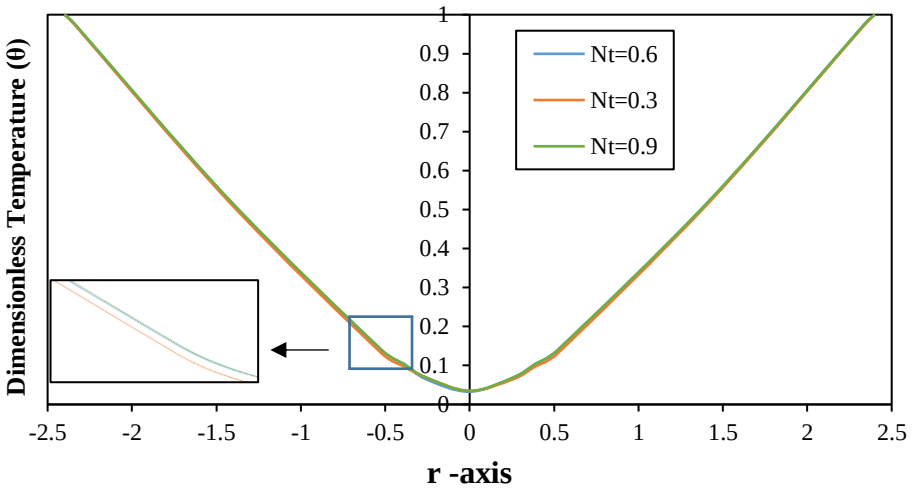

Figure 6 Effect of ***Nt*** on temperature distribution at the aneurysm in core region for *Gr = 2.0, N = 0.2, Nb = 0.6 and z = 10.80*

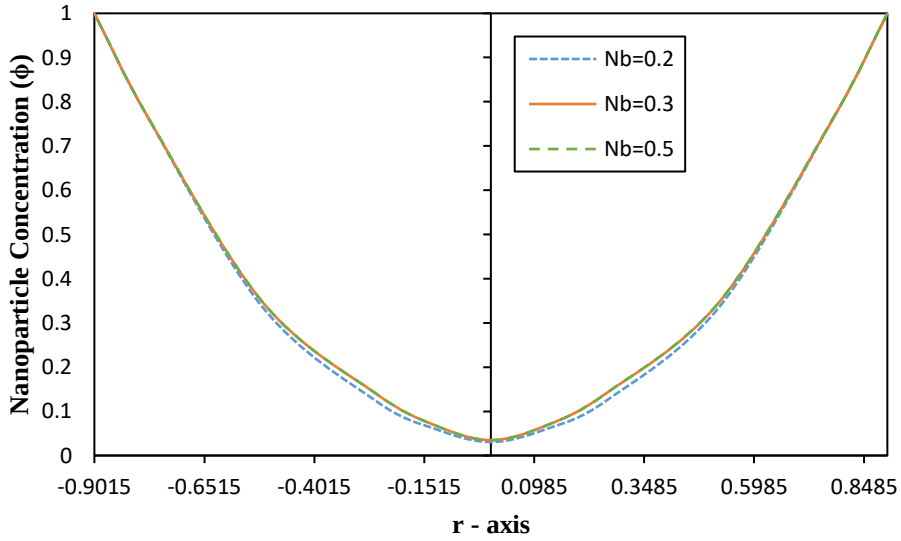

Figure 7 Effect of ***Nb*** on temperature distribution at the stenosis in core region for *Gr = 1.0, N = 0.2, Nt = 0.3 and z = 3.20*

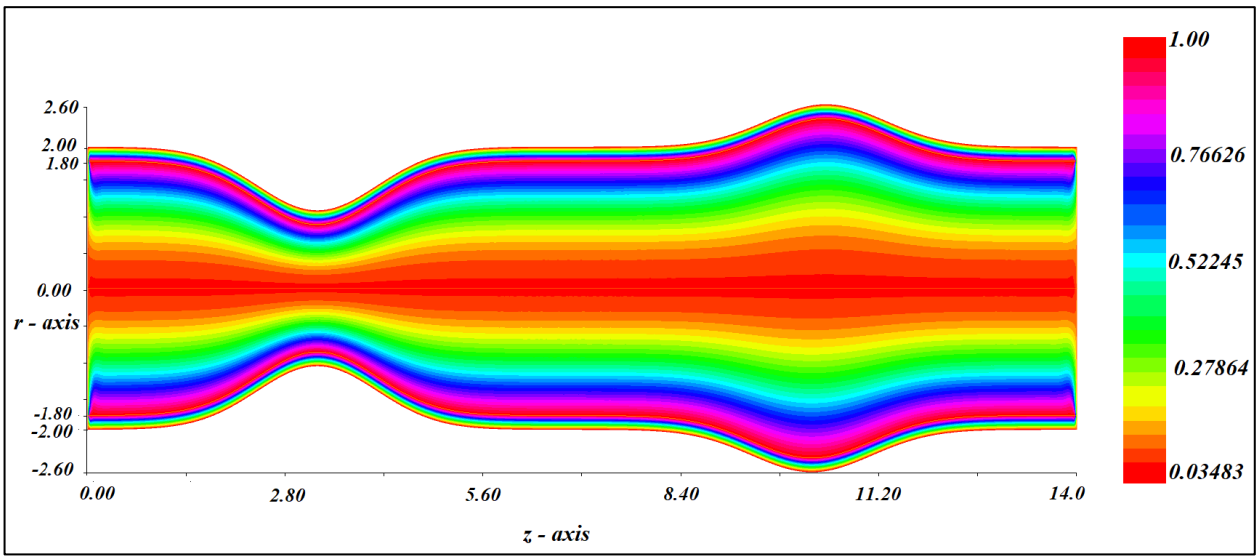

8(a)

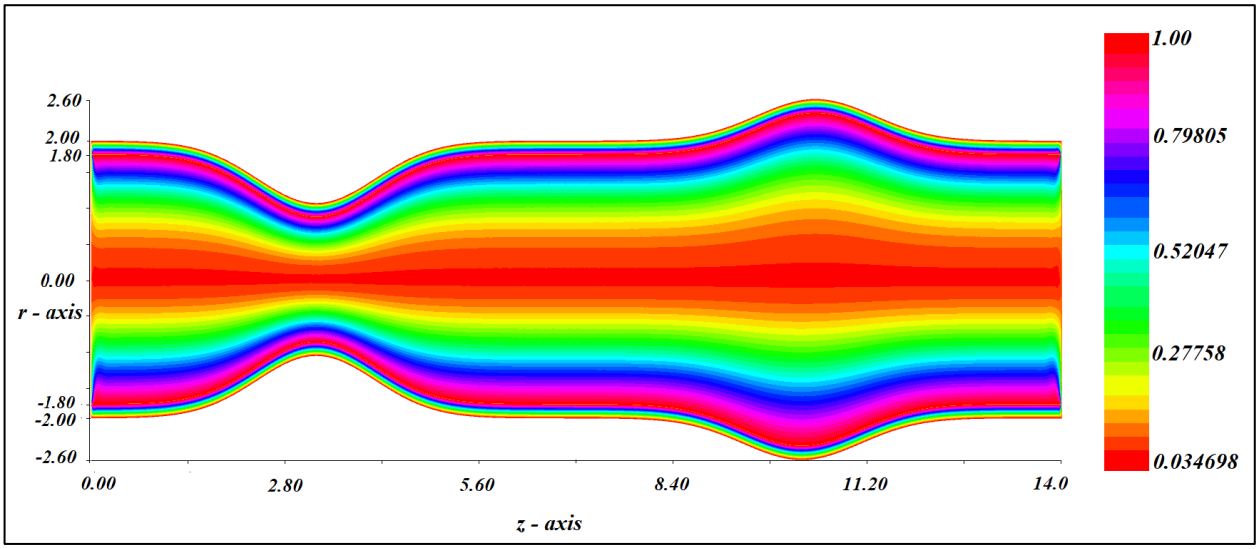

8(b)

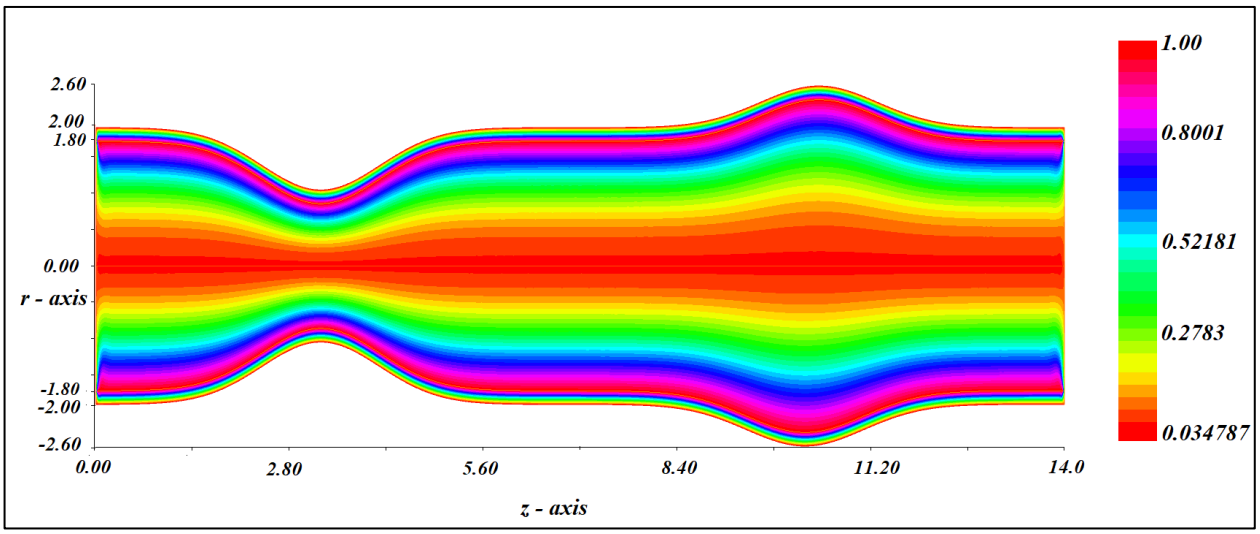

8(c)

Figure 8 Temperature distribution in the core region in arterial segment at **(a)** *Gr = 1.0, N = 0.5, Nt = 0.3 and Nb = 0.2***(b)** *Gr = 1.0, N = 0.5, Nt = 0.3 and Nb = 0.3* and **(c)** *Gr = 1.0, N = 0.5, Nt = 0.3 and Nb = 0.5.*

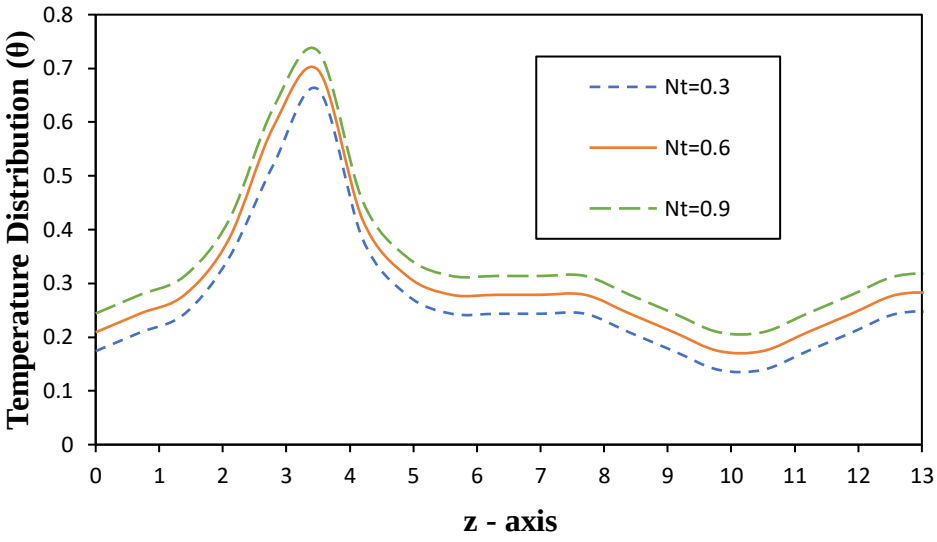

Figure 9 Effect of ***Nt*** on temperature distribution in core region for *r = 0.78, Nt = 0.3, Gr = 1.0 and N = 0.2*

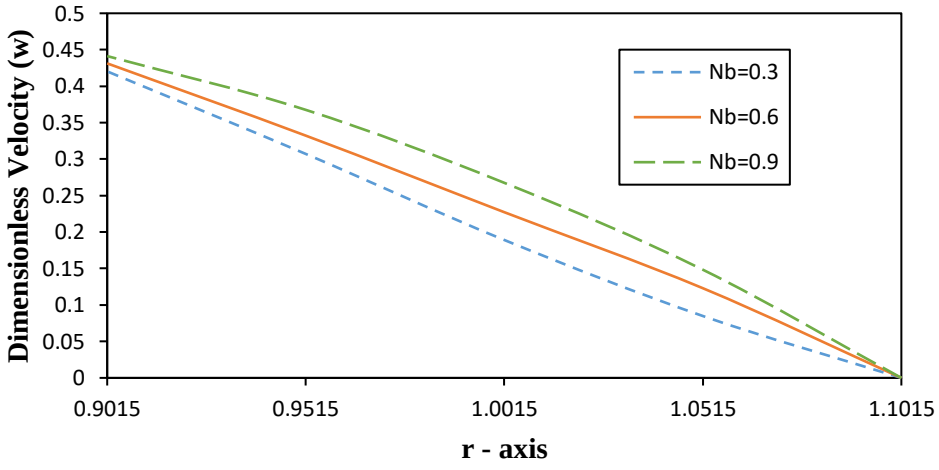

Figure 10 Effect of ***Nb*** on velocity field at stenosis in porous region for Gr = 1.0, N=0.2, *Nt = 0.3 and z= 3.20*

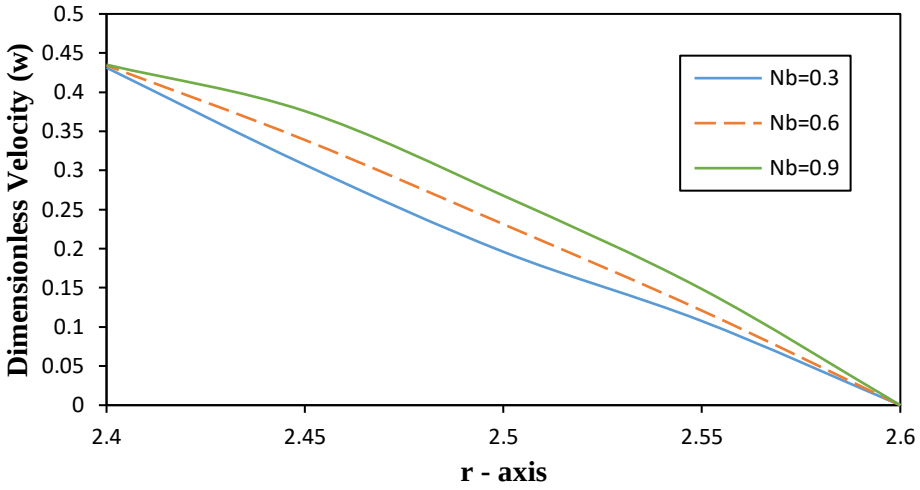

Figure 11 Effect of ***Nb*** on velocity field at aneurysm in porous region for Gr = 1.0, N=0.2, *Nt = 0.3 and z= 10.80*

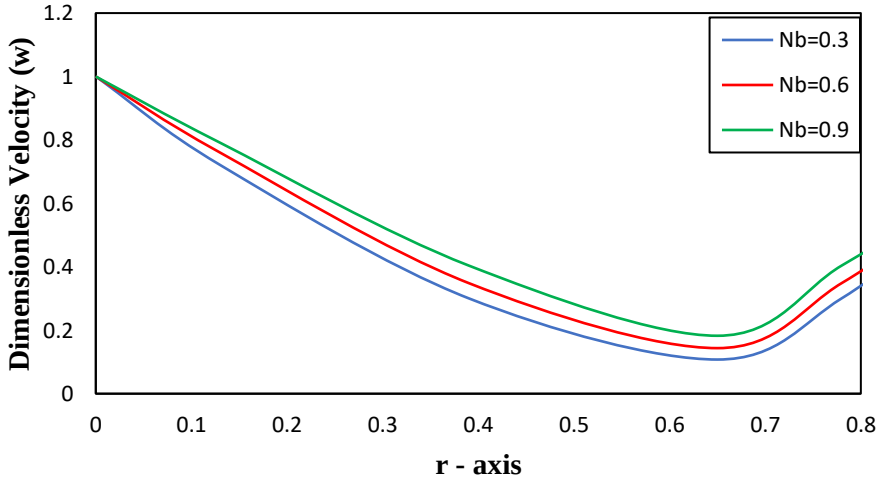

Figure 12 Effect of ***Nb*** on velocity field at stenosis in core region for *Gr = 1.0, N = 0.2, Nt =0.3 and z = 3.20*

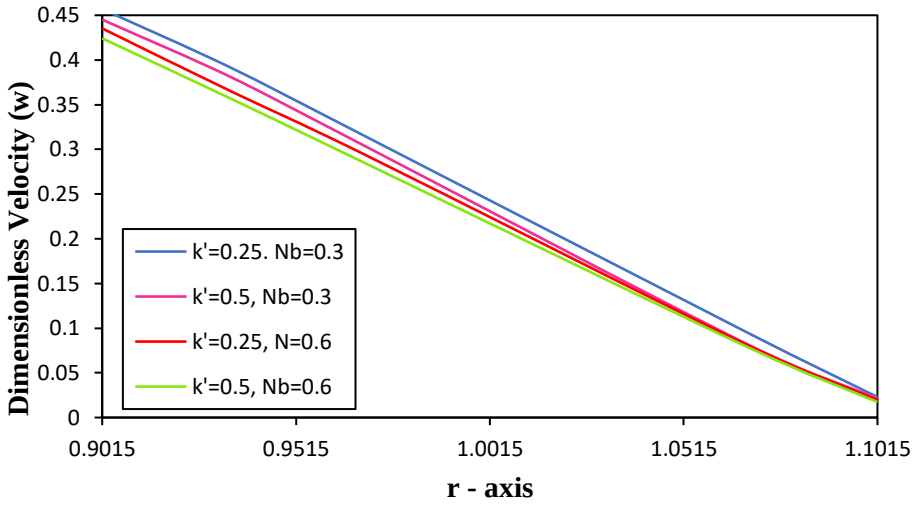

Figure 13 Effect of ***k'*** and ***Nb*** on velocity field at stenosis in porous region for *Gr = 1.0, N=0.2, Nt = 0.3, m = 0.657 and z = 3.20*

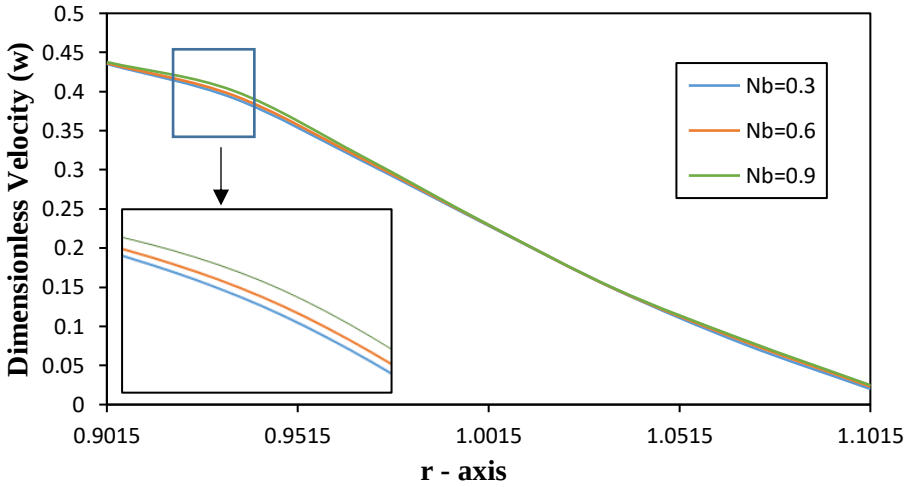

Figure 14 Effect of ***Nb*** on velocity field at stenosis in porous region for *Gr = 1.0, N=0.2, Nt = 0.3, m = 0.957, $k^{'}$ = 0.5 and z = 3.20*

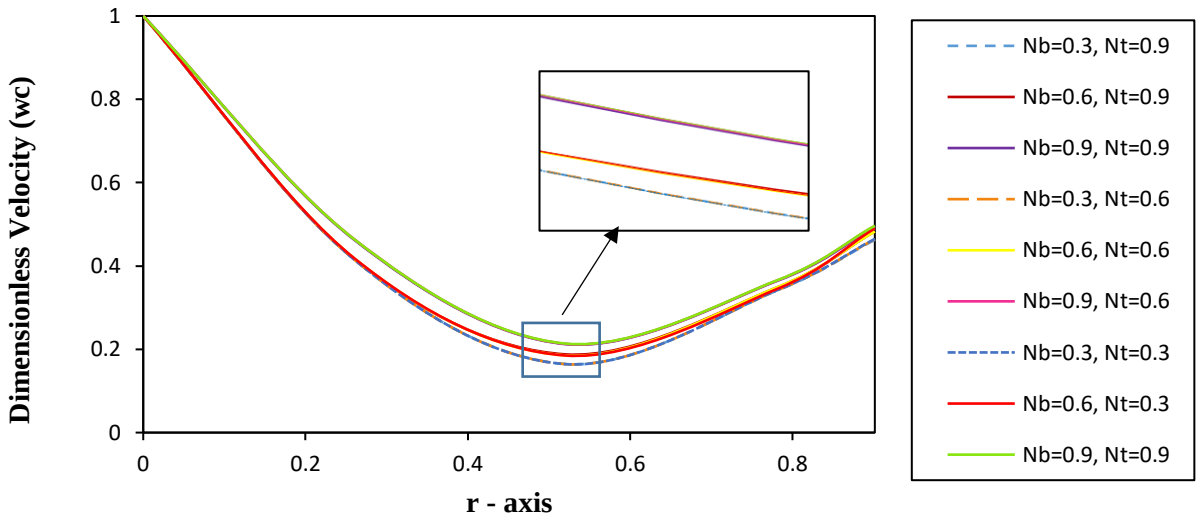

Figure 15 Effect of ***Nb*** and ***Nt*** on velocity field at stenosis in core region for *z=3.20, Gr=2.0, N=0.2*

Table 5: Volumetric flow rate at aneurysm for core region i.e. *m = 0.657, k' = 0.25, Gr = 1.0 N = 0.2 and Nt = 0.3*

Parameters (Fixed Values)	**Axial Value (z)**	**Volumetric flow Rate (Q)**		
		Parameter Value (Nb = 0.3)	***Parameter Value (Nb = 0.6)***	***Parameter Value (Nb = 0.9)***
Gr = 1.0, N = 0.2 and Nt = 0.3	2.4	0.178944	0.185886	0.177831
	2.34	0.329797	0.329165	0.31755
	2.21	0.44996	0.447032	0.43361
	2.08	0.542061	0.541297	0.52788
	1.95	0.608724	0.614043	0.602231
	1.82	0.652571	0.65277	0.645442
	1.69	0.676228	0.675186	0.673409
	1.56	0.650828	0.683377	0.688004
	1.43	0.611975	0.679425	0.691096
	1.3	0.564563	0.644594	0.665852
	1.04	0.454349	0.561695	0.601383
	0.9015	0.421472	0.530305	0.577393
	0.78	0.400279	0.509398	0.562247
	0.65	0.389695	0.507574	0.563652
	0.52	0.391726	0.510304	0.568517
	0.39	0.405058	0.523884	0.583388
	0.26	0.424444	0.544001	0.604523
	0.13	0.436762	0.557185	0.617906
	0	0.436762	0.557185	0.617906

Table 6: Volumetric flow rate at stenosis in the core region when *m = 0.657, k' = 0.25, Gr = 1.0 N = 0.2 and Nt = 0.3*

Parameters (Fixed Values)	**Axial Value (z)**	**Volumetric flow Rate (Q)**		
		Parameter Value (Nb = 0.3)	***Parameter Value (Nb = 0.6)***	***Parameter Value (Nb = 0.9)***
Gr = 1.0, N = 0.2 and Nt = 0.3	0.9015	0.067216	0.066798	0.040855
	0.78	0.101754	0.107758	0.063703
	0.65	0.110853	0.118515	0.077534
	0.52	0.12338	0.12338	0.084431
	0.39	0.140649	0.129834	0.095855
	0.26	0.157411	0.145358	0.113889
	0.13	0.168416	0.156861	0.127073
	0	0.168416	0.156861	0.127073

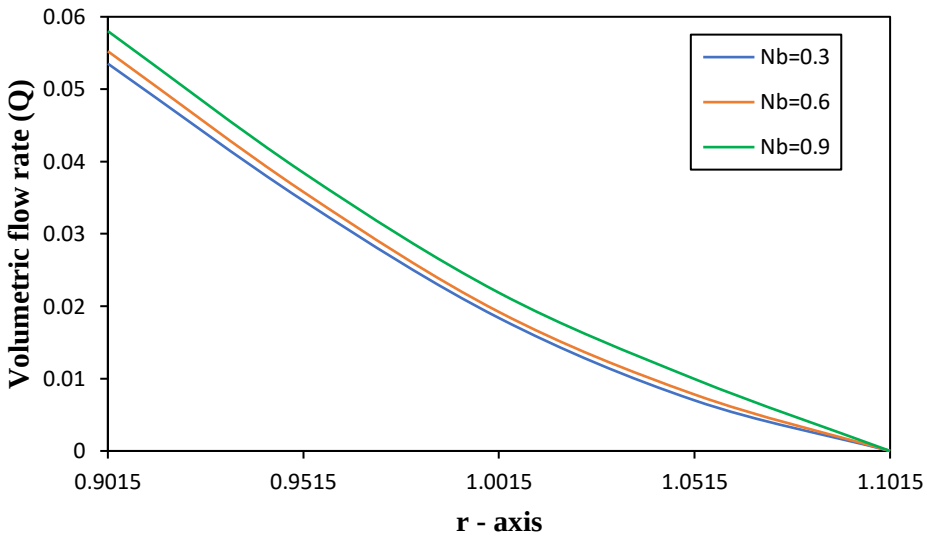

Figure 16 Effect of ***Nb*** on the volumetric fluid flow rate at stenosis in porous region for *Gr = 1.0, N = 0.2, Nt = 0.3,* and *z = 3.20*

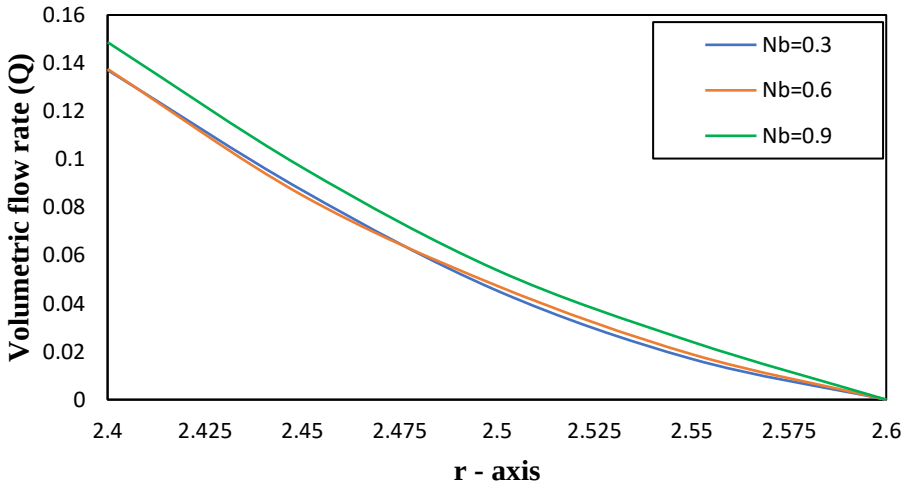

Figure 17 Effect of ***Nb*** on the volumetric fluid flow rate at Aneurysm in porous region for *Gr = 1.0, N=0.2, Nt = 0.3 and z =10.80*

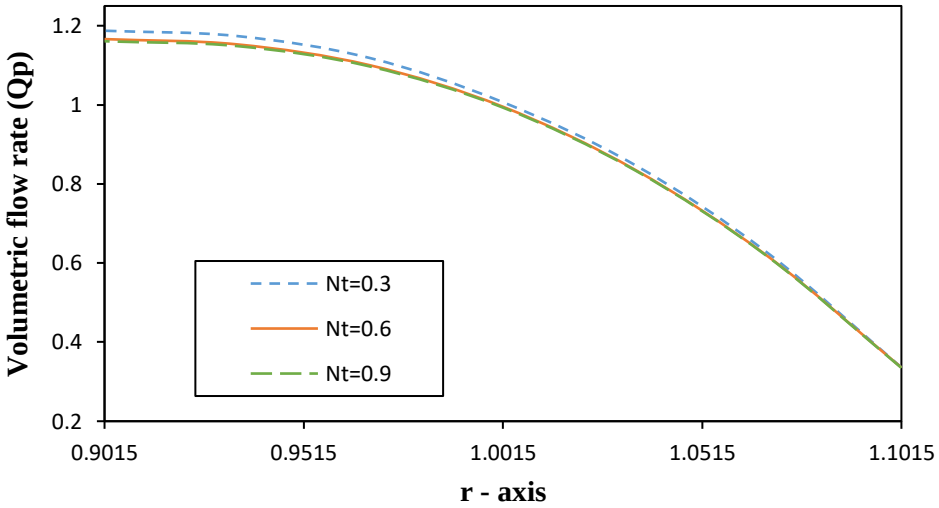

Figure 18 Effect of ***Nt*** on the volumetric fluid flow rate at stenosis in porous region for *N = 0.2, Gr = 1.0, Nb = 0.3 and z = 3.20*

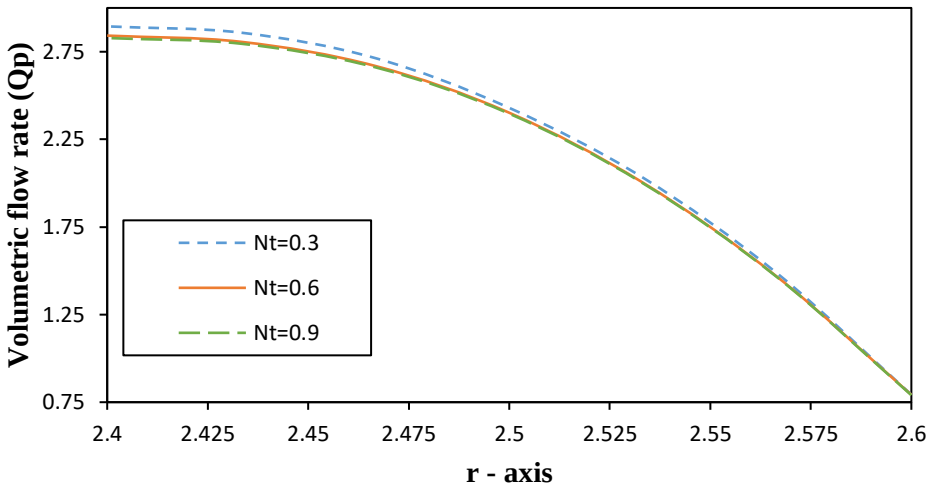

Figure 19 Effect of ***Nb*** and ***Nt*** on the volumetric fluid flow rate at aneurysm in porous region for *N = 0.2, Gr = 1.0, Nb = 0.3 and z = 10.80*

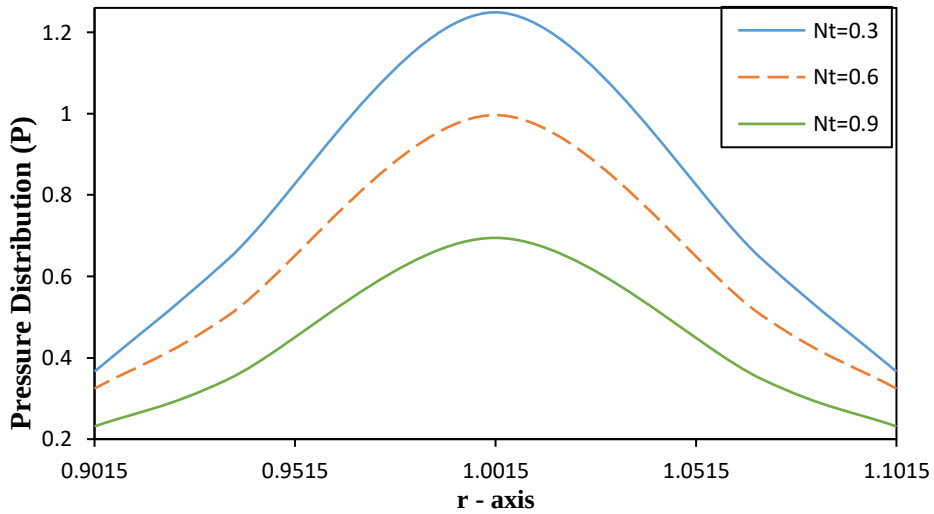

Figure 20 Effect of ***Nt*** on the pressure distribution at stenosis in porous region for *N = 0.2, Gr = 1.0, Nb = 0.3 and z = 3.20*

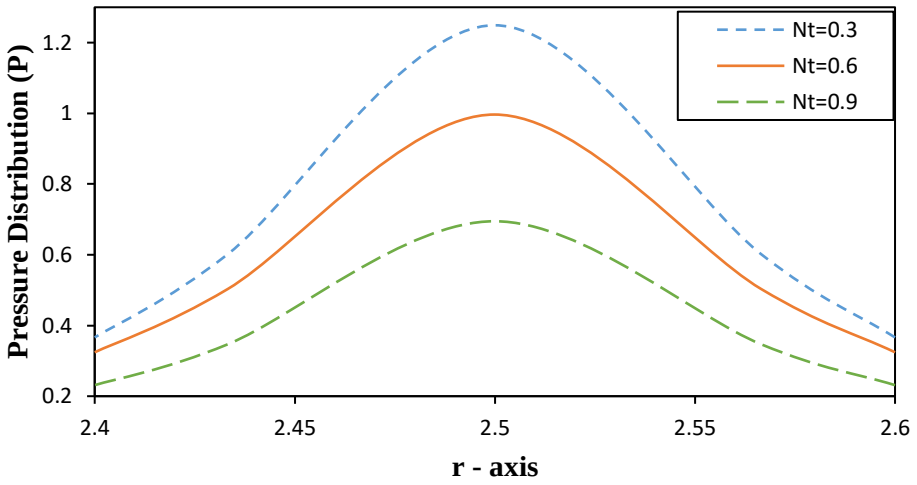

Figure 21 Effect of ***Nt*** on the pressure distribution at aneurysm in porous region for *N = 0.2, Gr = 1.0, Nb = 0.3 and z = 10.80*

Table 7: Numerical values of local skin friction coefficient $\frac{1}{2}\mathrm{Re}C_f^*$ for various values of *Nb* and *Nt* at stenosis (inner wall).

Parameters (Fixed values)	***Parameter Values (Nb)***	***Parameter values (Nt)***	***Local skin-friction coeff (C_f) (Stenosis)***	***Local skin-friction coeff (C_f) (Aneurysm)***
m=0.657, Gr=5.0 and N=0.2	0.3	0.3	0.46159	1.395
		0.6	0.48529	1.4291
		0.9	0.49494	1.4683
	0.6	0.3	0.40502	1.3147
		0.6	0.41523	1.3384
		0.9	0.43502	1.365
	0.9	0.3	0.33169	1.1736
		0.6	0.34413	1.292
		0.9	0.37089	1.2934

Table 8: Numerical values of local skin friction coefficient $\frac{1}{2}\mathrm{Re}\,C_f^*$ for various values of *Nb* and *Nt* at stenosis (outer wall).

Parameters (Fixed values)	*Parameter Values (Nb)*	*Parameter values (Nt)*	*Local skin-friction coeff. (C_f) (Stenosis)*	*Local skin-friction coeff. (C_f) (Aneurysm)*
m=0.657, Gr=1.0 and N=0.2	0.3	0.3	1.7619	3.5328
		0.6	1.8834	3.7668
		0.9	2.0229	4.0458
	0.6	0.3	1.4672	2.9524
		9.6	1.5606	3.1211
		0.9	1.6551	3.3102
	0.9	0.3	1.3322	2.6643
		0.6	1.4008	2.801
		0.9	1.4447	2.8894

Table 9: Numerical values of Nusselt number $Nu^{'}\mathrm{Re}$ for various values of *Gr, Nb and Nt* at stenosis (inner wall).

Parameters (Fixed Values)	*Parameter Values (Nb)*	*Parameter Values (Nt)*	*Nusselt Number ($Nu^{'}\mathrm{Re}$) (Stenosis)*	*Nusselt Number ($Nu^{'}\mathrm{Re}$) (Aneurysm)*
m=0.657, Gr=5.0 and N=0.5	0.3	0.3	2.479	2.479
		0.6	2.3522	2.3522
		0.9	2.31	2.31
	0.6	0.3	3.2359	3.2359
		0.6	2.729	2.729
		0.9	2.5601	2.5601
	0.9	0.3	3.3566	3.3566
		0.6	2.9766	2.9766
		0.9	1.2643	1.2643
m=0.657, Gr=2.0 and N=0.5	0.3	0.3	3.7849	3.7849
		0.6	3.3628	3.3628
		0.9	2.2322	2.2322
	0.6	0.3	3.8521	3.8521
		0.6	3.533	3.533
		0.9	2.479	2.479
	0.9	0.3	4.8485	4.8485
		0.6	3.6147	3.6147
		0.9	3.2359	3.2359

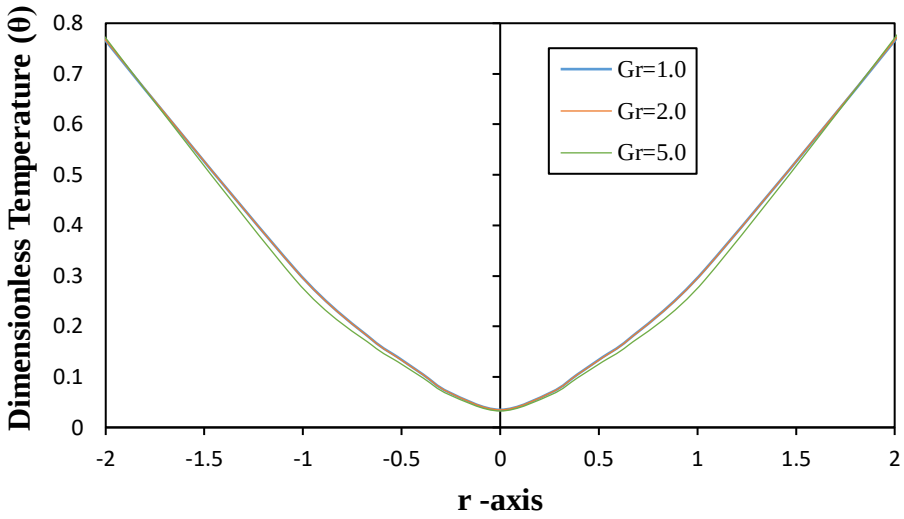

Figure 22 Effect of ***Gr*** on temperature distribution at Aneurysm in core region for *Nb = 0.3, Nt = 0.3, N = 0.2 and z = 10.80*

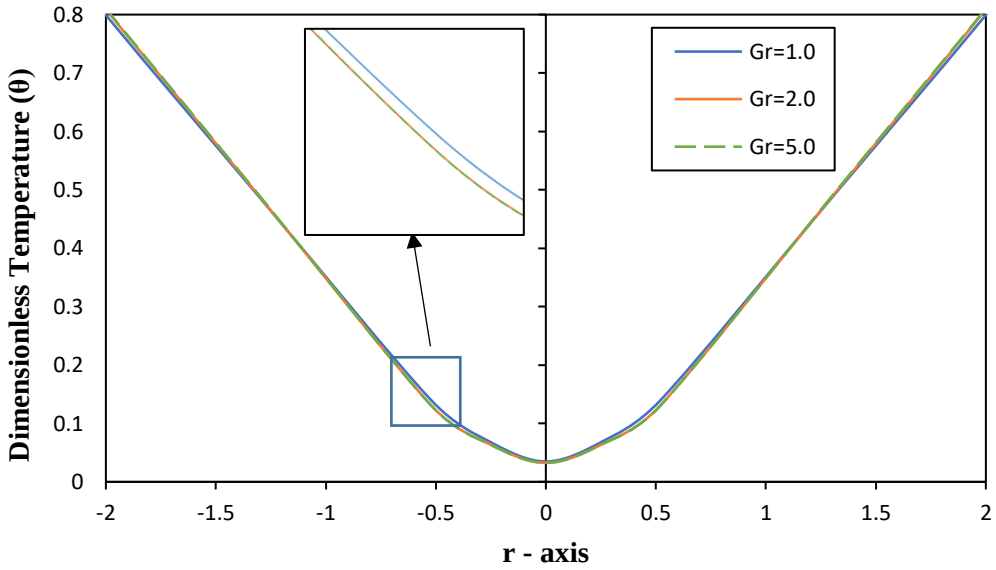

Figure 23 Effect of ***Gr*** on temperature distribution at Aneurysm in core region for *Nb = 0.3, Nt = 0.6, N = 0.2 and z = 10.80*

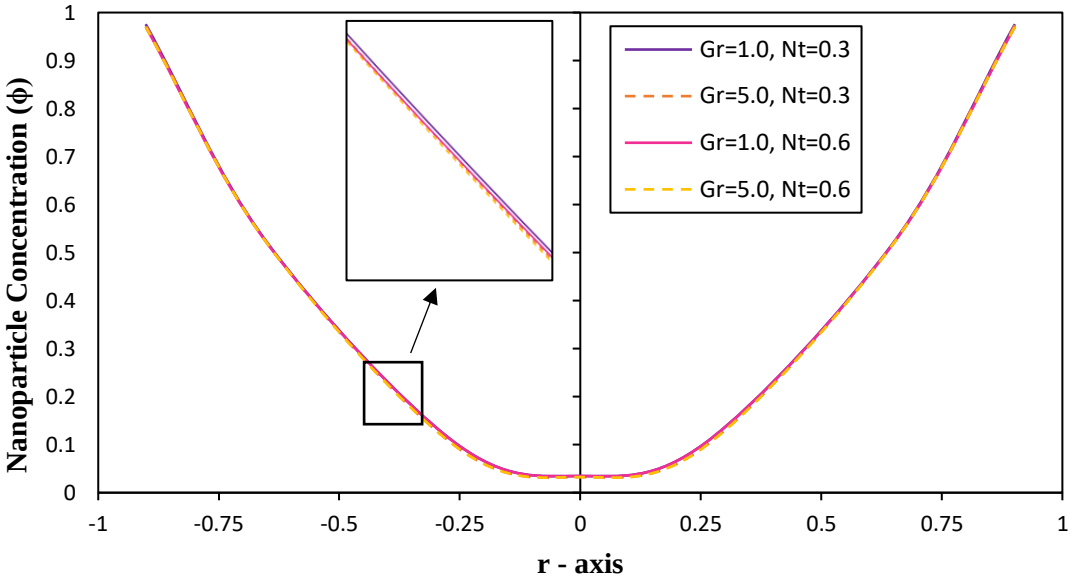

Figure 24 Effect of ***Gr*** and ***Nt*** on nanoparticles concentration at stenosis in core region for *Nb = 0.3, N = 0.2 and z = 3.20*

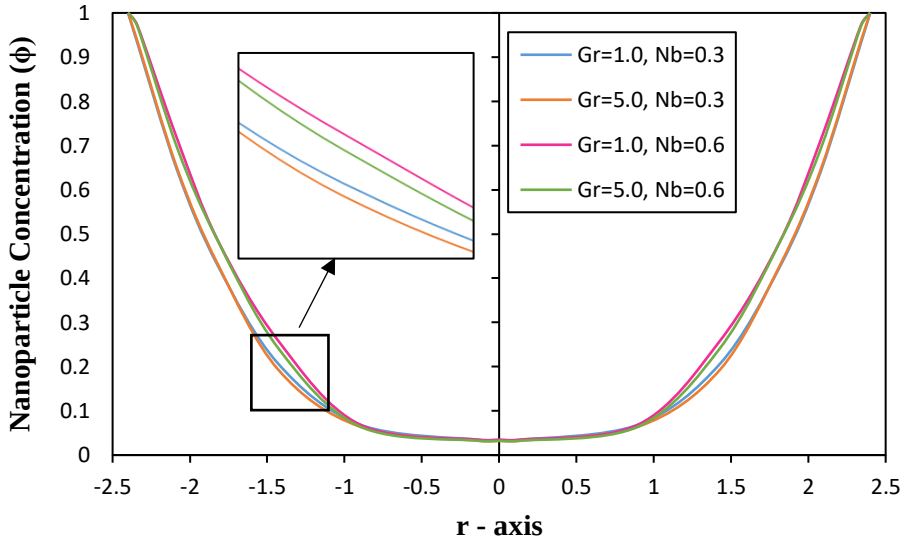

Figure 25 Effect of ***Gr*** and ***Nb*** on nanoparticles concentration at aneurysm in core region for *Nt = 0.6, N = 0.2 and z = 10.80*

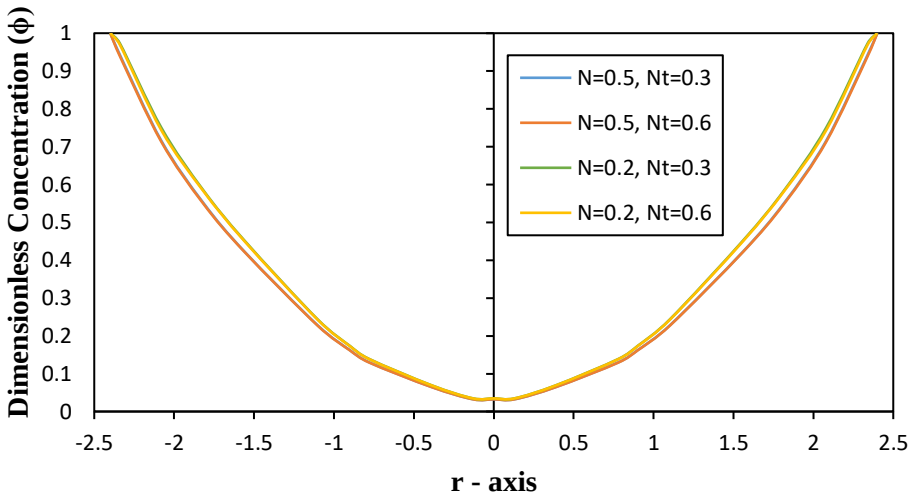

Figure 26 Effect of ***N*** and ***Nt*** on nanoparticles concentration at aneurysm in core region for *Nb = 0.6, Gr = 2.0 and z = 10.80*

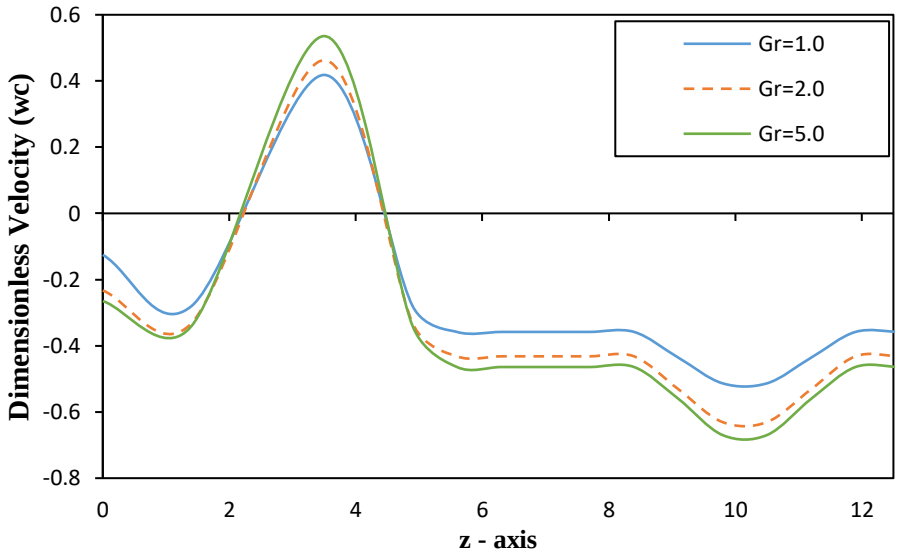

Figure 27 Effect of ***Gr*** on velocity field in core region for *Nb = 0.3, Nt = 0.3, N = 0.2 and r = 0.9015*

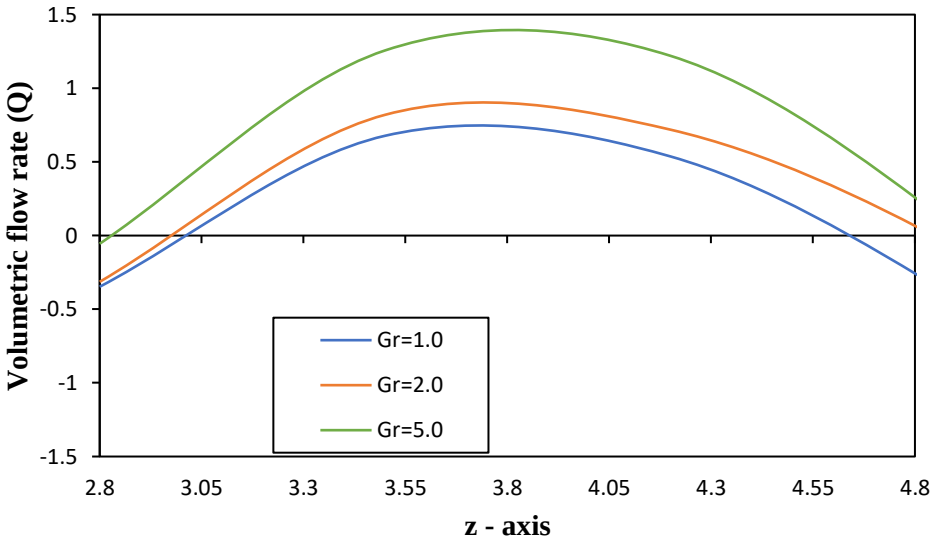

Figure 28 Effect of ***Gr*** on volumetric fluid flow rate at stenosis in core region for *Nb = 0.3, Nt = 0.3, N = 0.2, m =0.657, μ^* = 2.4 and r = 0.9015*

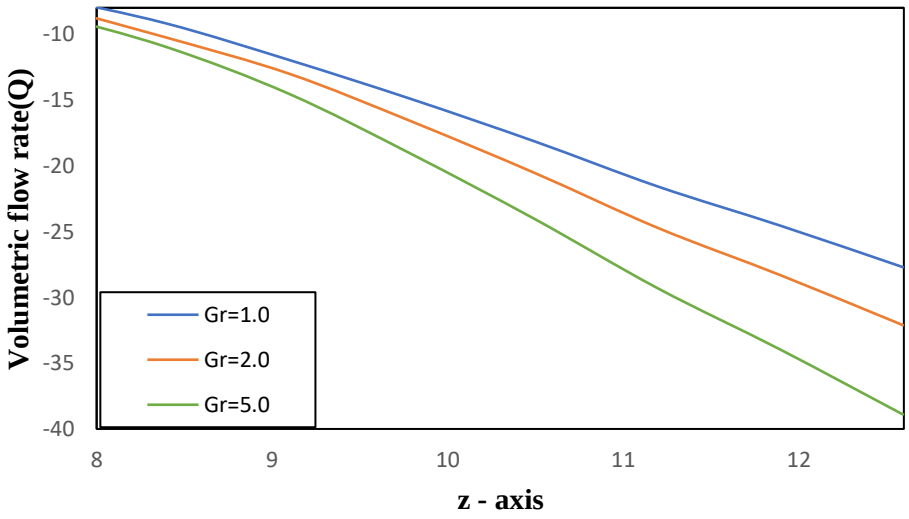

Figure 29 Effect of ***Gr*** on volumetric fluid flow rate at Aneurysm in core region for *Nb = 0.3, Nt = 0.3, N = 0.2, m =0.657, k' = 0.5 and r = 0.9015*

Table 10: Resistance impedance of blood flow in the artery at *Nb = 0.3, Nt = 0.3 and r = 0.9015*

Parameter (Fixed Values)	*Axial Values (z)*	*Resistance Impedance (λ)*		
		Parameters (Gr=1.0, N=0.2)	**Parameters (Gr=2.0, N=0.2)**	**Parameters (Gr=5.0, N=0.2)**
Nb = 0.3, N_t = 0.3 and r = 0.9015	**0.0**	0	0	0
	0.7	2.316125	2.09307	1.95986
	1.4	3.301795	2.92649	2.73952
	2.1	3.873804	3.416469	3.328878
	2.8	5.043784	4.713639	11.14221
	3.5	4.443586	4.216717	10.79782
	4.2	3.687537	3.650179	10.4432
	4.9	4.64422	8.714469	19.01652
	6.3	4.866474	9.008856	19.2687
	7.0	4.997242	9.132734	19.38745
	7.7	5.075965	9.208106	19.46066
	8.4	5.133265	9.260787	19.51254
	9.1	5.177449	9.300444	19.55192
	9.8	5.211389	9.331724	19.58164
	10.5	5.23855	9.356163	19.60424
	11.2	5.260923	9.375963	19.62221
	11.9	5.279753	9.392429	19.63697
	12.6	5.296298	9.406805	19.6497
	13.3	5.310958	9.419479	19.66141
	14.0	5.324043	9.430747	19.67122

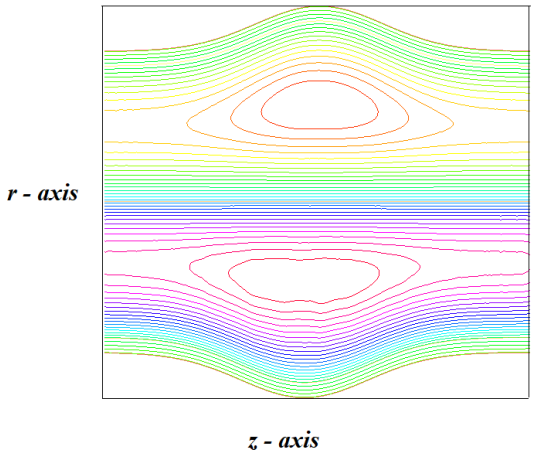

30(a)

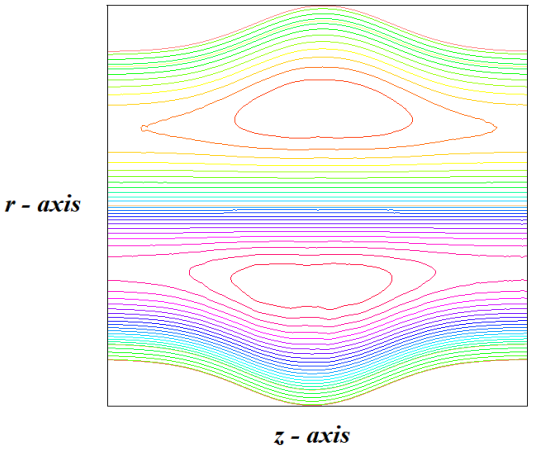

30(b)

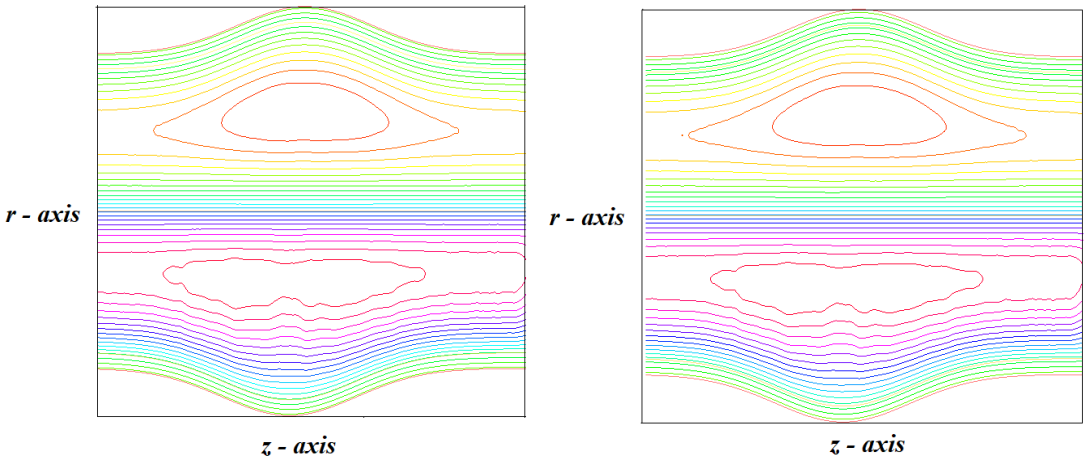

30(c) **30(d)**

Figure 30 Velocity Streamlines (Aneurysm) at **(a)** $Gr = 5.0, N = 0.2, Nb = 0.3,$ *and* $Nt = 0.3$, **(b)** $Gr = 5.0, N = 0.2, Nb = 0.6,$ *and* $Nt = 0.3$ **, (c)** $Gr = 5.0, N = 0.2, Nb = 0.6,$ *and* $Nt = 0.6$ **, (d)** $Gr = 5.0, N = 0.2, Nb = 0.6,$ *and* $Nt = 0.9$

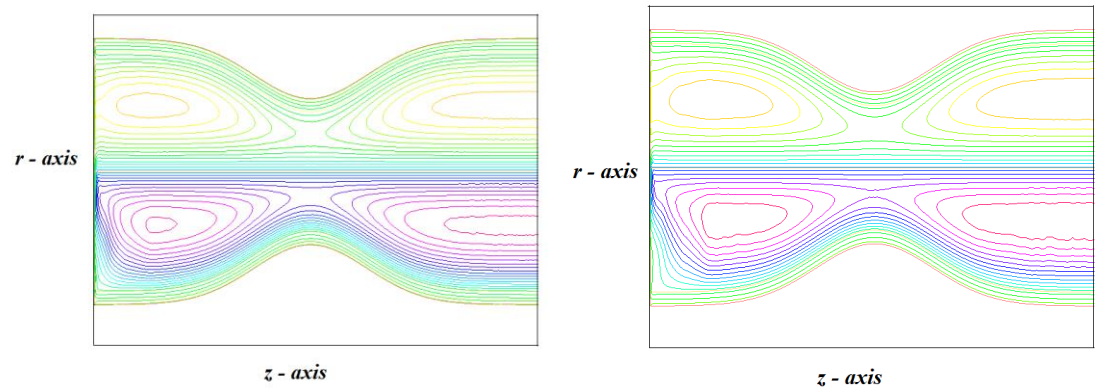

31(a) **31(b)**

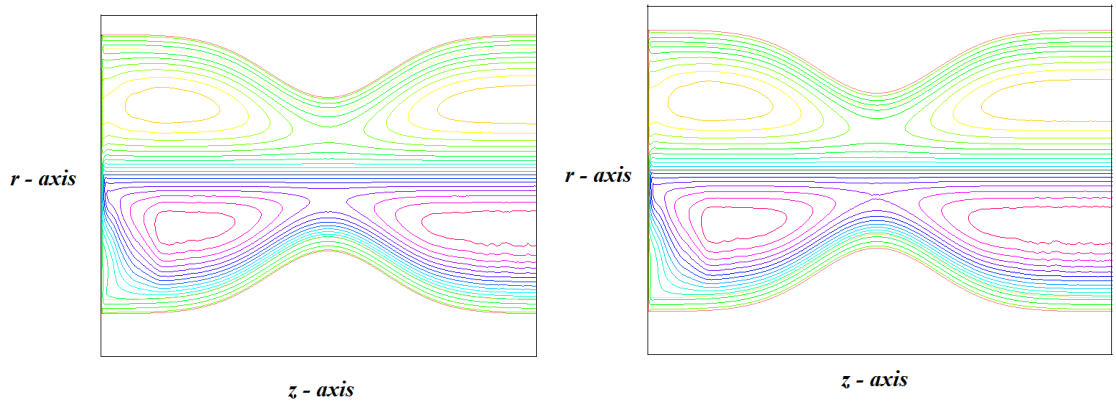

31(c) **31(d)**

Figure 31 Velocity Streamlines (Stenosis) at **(a)** $Gr = 5.0, N = 0.2, Nb = 0.3,$ *and* $Nt = 0.3$**,** **(b)** $Gr = 5.0, N = 0.2, Nb = 0.6,$ *and* $Nt = 0.3$ **, (c)** $Gr = 5.0, N = 0.2, Nb = 0.6,$ *and* $Nt = 0.6$, **(d)** $Gr = 5.0, N = 0.2, Nb = 0.6,$ *and* $Nt = 0.9$

To validate the scheme which has been adopted to simulate the current problem, the analytical results obtained by Ellahi et al. [73] for temperature of viscous blood flow are compared with the results obtained by using FEM for the model discussed by Ellahi et al. [73] and both are benchmarked with the current FREEFEM++ solutions, as displayed in table 3.It is evident that the results acquired by using the analytical method (HPM) and the FEM (variational approach) match up to three decimal points and both concur with the FREEFEM++ solution. Hence it can be deduced that the FREEFEM++ code is very accurate and suitable for this type of hemodynamic simulation.

.

5.1 Effect of Brownian motion parameter (Nb) and thermophoresis parameter (Nt)

The impact of Brownian motion parameter *Nb* and thermophoresis parameter (*Nt*) on temperature profile and nanoparticle concentration is shown in the different graphs and tables with the variation in radial coordinates. **Fig. 4 and 5** depict the influence of thermophoresis parameter (*Nt*) and Brownian motion parameter (*Nb*) on radial distribution of the nano-particle concentration (ϕ) at the throat of the stenosis and in the whole arterial segment with the fixed value of Grashof number (*Gr=1.0*), and solutal to thermal buoyancy ratio (*N=0.5*) in the core region. Similarly, with a change in thermophoresis parameter (*Nt*) there is ~ 0.36% decrement in magnitudes of nano-particle concentration for all radial coordinate values when *Nt* increases from *0.3* to *0.6*. Figure 5 illustrates the axial variation of nanoparticles concentration distribution and maximum concentration (volume fraction) arises at the stenotic arterial segment and decreases substantially in the aneurytic region. There is a marked elevation in the magnitudes of nano-particle concentration for all axial coordinates with ~5% increment when increasing Brownian motion parameter from 0.3 to 0.6 and then ~10% increment when increasing the Brownian motion parameter from 0.6 to 0.9 respectively. Both nanoscale effects generally assist in the diffusion of the nano-particle species at all radial coordinates although the effect is maximized at intermediate distances from the arterial mid-line. Brownian motion acts to distribute the nano-particles as uniformly as possible throughout the blood flow regime. This reduces the nanoparticle concentration *gradient* and diminishes the regional variations in fluid characteristics whereas it mobilizes species diffusion leading to an elevation in nano-particle concentration magnitudes.

Table 4 shows the effect of Brownian motion and thermophoresis parameters on the nanoparticle concentration distribution in the arterial segment. There is a noticeable elevation in nanoparticles concentration at the throat of stenosis induced with increment in Brownian motion parameter whereas the converse effect is generated with increasing thermophoresis parameter, when the

Grashof number (*Gr=1.0*) and buoyancy ratio (*N=0.5*). Relatively low sensitivity in nanoparticles concentration to alteration in thermophoresis parameter (*Nt*) is computed whereas there is a weak enhancement in concentration with larger Brownian motion effect (*Nb*).

Figures 6 and 7 are graphical representations of temperature distribution in blood flow with respect to radial coordinate for various values of thermophoresis parameter (*Nt*) and Brownian motion parameter (*Nb*) respectively. Figure 6 is drawn for the fixed values of *Gr = 2.0, N = 0.2 and Nb =0.3* whereas figure 7 is drawn for the fixed values of *Gr = 1.0, N = 0.2 and Nt =0.3.* Figure 9 visualizes temperature distribution in the blood flow with respect to axial coordinate for various values of thermophoresis parameter and is plotted with *Gr = 2.0, N = 0.2 and Nb =0.3*. A parabolic distribution is computed in Fig. 6 at the aneurysm and exhibits an increment in temperature magnitudes in the arterial segment with increasing value of thermophoresis parameter from *Nt = 0.3 to Nt =0.6*. Fig. 7 shows the comparison of computation done at stenosis and indicates that the temperature increases with an increment in the Brownian motion parameter (*Nb*). Higher values of nanoscale thermophoresis parameter (*Nt*) induces a slight enhancement in temperatures at all radial locations of the arterial vessel; however, the principal elevation is only observed around the central zone and diminishes progressively toward the vessel inner boundaries. Similarly, inspection of the coloured contours presented in Figure 8(a)-8(c), reveals that temperature increases with both an increase in thermophoresis parameter (*Nt*) and Brownian motion parameter (*Nb*). The increment in Brownian motion parameter *Nb* is from *0.2 to 0.3* and then from *Nb = 0.3 to Nb = 0.5; at Nt =0.3*, the temperature increasees at the wall as well as in the centreline region. The temperature magnitudes are greater near the inner wall of the artery in comparison to the midline which is attributable to the increment in *Nb* decreasing the thermal conductivity of the base fluid. The thermophoretic force due to temperature gradient, causes a rapid migration of heat from the midline. Therefore, hot fluid is moved away from the centreline, and the thermal boundary layer becomes thicker**. Fig. 9** further shows that significant heating of the blood is generated i.e. higher temperatures generated with an increase in the thermophoresis parameter. Again, the deviation from axisymmetric distributions (observed in unobstructed vessels) is clearly captured in this figure (for the core region) confirming the significant influence of the stenosis and aneurysm on distorting temperature distributions in diseased (obstructed) arteries. Considerable elevation in temperature is seen in the vicinity of the stenosis whereas there is depletion in the aneurysm location.

Figs. 10- 12 show the velocity profile distributions with variation of Brownian motion parameter (*Nb*) in both the regions i.e., core region and peripheral region (porous region) for the dual cases

of stenosis and aneurysm respectively. There is a distinct elevation computed in velocity (i.e. flow acceleration is produced) in the porous region with increasing Brownian motion parameter (progressively smaller nanoparticles) in both figures 9 and 10 at the stenosis and aneurysm, respectively (corresponding to the peripheral region). The velocity field exhibits a difference only near the inner wall but shows equal decrement to the outer wall of the artery for all values of *Nb* in both the constriction (stenosis) and dilation (aneurysm). Increment in Brownian motion parameter enhances the mobility of the nanoparticles which encourages ballistic collisions and momentum diffusion in the hemodynamic flow and this manifests in flow acceleration. However, owing to the greater resistance to blood flow while moving from inner wall to outer wall in the peripheral region, there is an exaggerated velocity variation near the inner wall. Figure 11 is a graphical representation of the velocity field in the *core region* for the stenosis. Clearly velocity increases with Brownian motion parameter but it shows some different variations in comparison to the nanoparticle concentration and temperature. The velocity field generally decreases while approaching the artery boundary (wall) and in closer proximity to the wall is observed to increase. The velocity field is maximum along the arterial centre line (r=0) and decays towards the wall. However, the presence of nanoparticles leads to an acceleration near the wall and a reduction in the momentum boundary layer thickness there.

Figs. 13 presents the evolution in radial velocity distribution in the porous (peripheral) region for different value of permeability parameter (k'). While comparing both the figures it has been found that increment in permeability parameter (drag force) increases resistance to the flow which induces a decrement in velocity in the porous region i.e. blood flow retardation. Clearly porous effects are non-trivial and stronger at smaller values of radial coordinate in the peripheral zone.

Figs. 14-15 depict the velocity field variation at the peripheral and stenotic part of the arterial segment (core region), respectively, for different values of Brownian motion parameter (*Nb*) and thermophoresis parameter (*Nt*). A weak acceleration in the flow is induced with increasing *Nb*, in the peripheral region (Fig. 13) and the effect is most prominent at lower radial coordinate values. Fig. 14 shows that the velocity field increases in the core region with thermophoresis parameter and is less sensitive to Brownian motion parameter in this zone.

Tables 5 and 6 and **Figs 16-17** document and illustrate variation in volumetric flow rate (Q) in the arterial segment at stenosis and aneurysm in the porous (peripheral) region respectively for a modification in Brownian motion parameter (*Nb*). The flow rate is maximum at the mid-line of the artery and decreases as we move radially to the wall of the artery. The decay is smooth and undisturbed from the centre to the boundary. The flow rate is the summation of variable velocity

with the radial direction i.e., the integration of the velocity with respect to radial coordinate. Hence the flow rate shows similar behaviour to the velocity. Lower magnitudes of flow rate are however computed at the stenosis compared with the aneurysm, in particular at lower radial coordinate values.

Figs. 18-19 illustrate respectively the effect of thermophoresis parameter (*Nt*) and collective effect of Brownian motion (*Nb*) and thermophoresis parameters (*Nt*) on the volumetric flow rate (*Q*) again in the porous region at the stenosis and aneurysm locations. From the figures, it can be seen that, moving from inner wall to outer wall the flow rate is decreasing towards zero due to the no-slip velocity boundary condition and the flow rate decreases by increasing the values of thermophoresis parameter *Nt*. However larger magnitudes of flow rate correspond to the aneurysm (Fig. 19) and lower magnitudes to the stenotic region (Fig. 18). These different geometrical obstructions therefore do not exert the same influence on flow rates in the diseased artery.

Figs. 20-21 describe the influence of thermophoresis parameter (*Nt*) on pressure distribution in the porous region at the stenosis and aneurysm for fixed values of *Gr = 1.0 and N = 0.2* respectively. The pressure *decreases* significantly with a boost in thermophoretic body force but does not continuously rise with greater radial coordinate values. Pressure peaks at intermediate radial coordinate and thereafter decays with further increase in radial coordinate. Nanoscale effects (of which thermophoresis is merely one manifestation [41]-[44]) clearly modify the pressure distribution in diseased arterial blood flow and clearly undesirably high blood pressures may be controlled with the judicious deployment of nanoparticles in hemodynamics. This has important implications in promoting nano-pharmacodynamics as an effective technique for controlling hypertension and other ailments associated with stenotic arterial disease.

Tables 7-10 show the variation in values of local skin-friction coefficient for the stenosis and aneurysm in the core and porous region and Nusselt number in the core region, respectively. In **Table 7** it is evident that with increasing Brownian motion parameter (*Nb*) there is a marked suppression in local skin friction both at the stenosis and at the aneurysm although the decrement is more prominent for the former. With a boost in thermophoresis parameter (*Nt*), the reverse response is induced i.e. skin friction is elevated consistently indicating that flow acceleration is produced in the stenosis and aneurysm locations. Thermophoretic body force is therefore the primary mechanism for ensuring nanoparticles improve drug delivery in obstructed hemodynamics since it accelerates the flow (with an associated decrease in blood pressure). Preferential particle deposition is therefore an excellent mechanism for achieving improved delivery of pharmaceutical nanoparticles, achieving longer residence-time and targeting specific zones for mediated therapy

[74, 75]. In **Table 8** again the collective influence of Brownian motion parameter (*Nb*) and thermophoresis parameter (*Nt*) on local skin friction is given although for a much weaker thermal Grashof number (*Gr* = 1.0) compared with Table 7 (in which *Gr* = 5.0). In both tables the Sisko rheological parameter, *m* = 0.657 and *N* = 0.2, implying that the viscoelasticity is weak in the core arterial region and that nano-particle species buoyancy force is one fifth of the thermal buoyancy force). Much greater local skin friction magnitudes are observed in Table 8 indicating that weaker thermal buoyancy force (*Gr* = 1.0) implies the thermal buoyancy and viscous hemodynamic forces are equal) leads to a strong acceleration in the blood flow, both at the stenosis and the aneurysm. It is further of note that negative skin friction never arises in either Table 7 or 8 implying that despite the presence of a stenosis or aneurysm, *back flow is never generated* in the arterial domain. **Table 9** shows the results for Nusselt number in the core region (inner wall) at both the stenosis and aneurysm for two cases of Grashof number (*Gr* = 5.0 and 2.0) again with the influence of Brownian motion parameter (*Nb*) thermophoresis parameter (*Nt*). With larger *Nb* there is an elevation in local Nusselt numbers at both the stenosis and the aneurysm. Heat transfer to the arterial wall (inner) is therefore enhanced with more intense Brownian dynamics (smaller nanoparticles) since temperatures are decreased in the blood with this effect i.e. the blood is cooled. The contrary effect is generated with greater thermophoresis parameter i.e. *Nt, i.e. increasing Nt leads to a strong suppression in Nusselt number which is observed both in the stenotic and aneurysm zones.* With greater value of Grashof number there is a clear depression in Nusselt numbers i.e. heat transfer to the inner wall of the artery is significantly decreased. The greater thermal buoyancy effect is known to heat the blood flow and this transfers heat from the boundaries (walls) to the body of the fluid, manifesting in a plummet in heat transfer to the wall i.e. decreasing Nusselt numbers.

5.2 Effect of Grashof Number (Gr) and Buoyancy ratio parameter (N)

The effect of Grashof number (*Gr*) and solute: thermal buoyancy ratio (*N*) on the hemodynamic characteristics i.e. temperature, nanoparticle concentration, pressure distribution and velocity field are illustrated in **Figs. 22- 29**.

Figure 22-24 show the influence of Grashof number on profiles for temperature distribution for two different values of thermophoresis parameter (*Nt = 0.3 and 0.6*) at the aneurysm (axial location, *z* = 10.80). With elevation in Grashof number (Fig. 22) the temperature decreases near the mid-line (central zone) but it increases near the inner wall of the artery (large values of radial coordinate, *r*). Grashof number represents the ratio between the buoyancy forces due to spatial

variation in fluid density (caused by temperature differences) to the shearing force due to the viscosity of the fluid. An accentuation in thermal buoyancy will therefore enhance *temperature difference* resulting in cooling (decrement in temperature) near the arterial mid-line and heating (increment in temperature) near the inner wall of the artery. Thermal buoyancy therefore exerts some effect on thermal characteristics of the hemodynamics. The contribution from species buoyancy is also present, however it is much weaker than thermal buoyancy for the numerical experiments performed (N =0.2). A more prominent reduction in core temperatures is witnessed at the stenosis (Fig. 22) than at the aneurysm zone (Fig. 23), although the trends are similar at the stenosis and aneurysm both in proximity to the arterial centre line and the wall.

Figs. 24-25 visualize the nanoparticle concentration distributions with variation of Grashof number (Gr) and Brownian motion parameter (Nb) and thermophoresis parameter (Nt), at the stenosis and aneurysm respectively. In figure 24, for the stenotic zone, the increment in Grashof number weakly reduces the nanoparticle concentration near the wall and in the central zone of the arterial segment. The higher value of Grashof number implies a more dominant thermal buoyancy force which mobilizes stronger thermal convection currents in the blood flow, and this inhibits the diffusion of nanoparticles i.e. decreases concentration of nanoparticles. Increasing thermophoresis effect (Nt) also marginally reduces nano-particle concentrations in the blood since it promotes the migration of nanoparticles to the periphery away from the central zone. In fig. 25, for the aneurysm part of the artery, a significant variation in nanoparticle concentration is computed with a rise in Brownian motion parameter. The exacerbation in collisions of nanoparticles with Brownian dynamics (smaller nanoparticles correspond to larger values of Nb) leads to enhanced species diffusion and a boost in nanoparticle concentration i.e. volume fraction (~4%). However as noted at the stenotic region (Fig. 24) increasing Grashof number again generally suppresses the nanoparticle concentrations.

Fig. 26 presents the collective influence of solutal to thermal buoyancy ratio (N) and thermophoresis effect (Nt) on nanoparticle concentration (ϕ). Increasing the value of solutal to thermal buoyancy ratio (N) generates a reduction in nanoparticle concentration. Stronger species buoyancy force is associated with N = 0.5 whereas weaker species (solutal) buoyancy force is represented by N = 0.2. At the arterial walls, the species (nanoparticle) boundary layer thickness will also be reduced. There is also a much weaker decrement in nanoparticle concentration (ϕ) with greater thermophoresis effect.

Fig. 27 depicts the evolution in velocity field with axial coordinate at a fixed radial coordinate (r = 0.9015) *in the core region* (viscoplastic Casson fluid) with a change in Grashof number (Gr). It

is evident that at the stenosis the velocity is elevated (lower *z* value) whereas it is significantly decreased at the aneurysm location (higher z values) at all values of Grashof number. Increasing thermal buoyancy only accelerates the flow in the vicinity of the stenosis whereas everywhere else it results in strong flow deceleration. Momentum boundary layer thickness will therefore be reduced at the stenosis whereas the boundary layer thickness will be significantly increased downstream at the aneurysm. The impact of thermal buoyancy is therefore not consistent in the hemodynamic regime and care must be taken in deploying nano-drugs to ensure that the desired effect is achieved whether at the entry zone, stenosis, aneurysm or indeed any other location in the target zone for the treatment. Figs 28 and 29 indicate that volumetric flow rate (*Q*) is consistently elevated in the core zone at the stenotic section with increasing Grashof number whereas it is depressed in the aneurysm zone. The *Q-z* profiles in Fig. 28 (stenosis) are clearly *inverted parabolas* whereas the *Q-z* profiles in Fig 29 (aneurysm) are approximately linear decays indicating that a very different interplay between flow rate and axial coordinate exists at the different arterial locations since the former is associated with a constriction (stenosis) whereas the latter is representing a dilatation (aneurysm) in the vessel geometry.

Table 9 documents the values of hemodynamic resistance (impedance) in the artery with respect to axial coordinate (z-axis) for the variation in Grashof number at fixed value of thermophoresis parameter and Brownian motion parameter i.e. (*Nb = 0.3, Nt = 0.3*). Resistance impedance of the fluid flow is associated with the ratio of negative of pressure gradient and fluid flow rate. Since the flow rate decreases while increasing the Grashof number in the aneurysm (*higher z-values s it is found further downstream of the stenosis*) and also the negative pressure gradient increases, this produces an increase in resistance impedance at the aneurysm with higher thermal buoyancy effect i.e. larger Grashof number. However, at the stenosis (lower *z*-values, as it is located further upstream of the aneurysm), the flow rate increases while increasing the Grashof number and also the pressure gradient increases. This effectively manifests in a decrement in resistance (impedance) with Grashof number increment. Therefore, lower hemodynamic impedance is observed at the aneurysm with greater thermal buoyancy effect. The inclusion of heat transfer in obstructed hemodynamic simulations is therefore proven to be a significant factor in predicting more accurately the characteristics of such flows. The *heat-conducting nature of blood* is fundamental to life-support and is well-documented in physiological and also pharmacological literature and is therefore strongly recommended for inclusion in mathematical/computational fluid dynamic models of stenotic/aneurysmic hemodynamics [76, 77].

In addition with these results it can also be pointed out that the skin–friction shows a decreasing behaviour as it is significantly more at inner boundary than outer boundary at stenosis and aneurysm both.

Finally, in **figs. 30-31**, to provide two-dimensional visualizations of the circulation hemodynamics in obstructed blood flow, contour plots have been presented for trapping. This describes an interesting phenomenon for the blood flow pattern and relates more to vorticity rather than velocity profiles. In particular it provides a good insight into occlusion effects in hemodynamics as represented by stenosis and aneurysm features. Figs. 30(a)-30(d), represents the streamlines of blood flow in the arterial domain *at the aneurysm* and figures 31(a)-31(d), represents the streamlines of blood flow in an artery *at the stenosis* both for the core region. In figures 30(a)-30(b) and 31(a)-31(b), it is observed that the magnitude of trapped boluses grows with an increase in the Brownian motion parameter for both obstruction cases i.e., stenosis and aneurysm. Clearly there are two trapped boluses in the stenotic zone but four in the aneurysm zone, at any Brownian motion number. Figs. 30(c)-30(d) and 31(c)-31(d), however shows that increasing thermophoresis parameter does not exert any tangible effect on bolus structure or quantity in either the stenosis or the aneurysm.

6. Conclusion

In this article, computational fluid dynamics modelling of steady-state, two-dimensional blood flow conveying spherical metallic nanoparticles in an arterial geometry with porous wall and featuring both a stenosis and aneurysm has been described. The objective has been to provide further refinement in simulating nano-pharmacological transport phenomena in the treatment of hemodynamic ailments (obstructed arteries etc). A Casson viscoplastic fluid model has been adopted for hemo-rheology in the core region and a Sisko viscoelastic fluid model in the peripheral (porous) region to represent non-Newtonian behaviour. The revised Buongiorno two component nanofluid model is employed for nanoscale effects. The governing equations have been derived by extending the Navier-Stokes equations with linear Boussinesq approximation (which simulates both heat and mass transfer). Natural (free) double-diffusive convection is considered to simulate the dual influence of thermal and solutal buoyancy forces. The dimensionless, transformed mass, momentum, energy and nano-species diffusion equations have been solved computationally with the powerful variational finite element method in the FreeFEM++ software. A comprehensive mesh-independence (grid sensitivity) study has been included. The effect of selected parameters (thermophoresis, Brownian motion, Grashof number, thermo-solutal buoyancy ratio, and Sisko

parameter ratio and permeability parameter) on velocity, temperature, nanoparticle concentration and hemodynamic pressure have been calculated for two clinically important cases of arteries with a stenosis and an aneurysm. Skin-friction coefficient, Nusselt number, volumetric flow rate and hemodynamic (resistance) impedance of blood flow are also computed. Colour contours and graphs are employed to visualize the simulated blood flow characteristics. The principal findings from the numerical simulations may be summarized as follows:

- It has been observed that in the core region moving from the inlet to the outlet, the nanoparticle concentrations increase with increasing the Brownian motion parameter. Also, the temperature increases noticeably when increasing the thermophoresis parameter.
- Coloured contours describes the enhancement in the temperature as increases in the thermophoresis parameter and Brownian motion parameter at both the stenosis and aneurysm while moving in radial direction.
- The velocity field increases with higher Brownian motion parameter (smaller nanoparticles) in the core region. In the porous (peripheral) region the flow is also accelerated (as in the core region) with increasing Brownian motion parameter at both the stenosis and aneurysm sections.
- The volumetric flow rate increases in the aneurysm region when increasing the Brownian motion parameter whereas it is suppressed near the inner wall. However, it exhibits a different response in the stenotic region since volumetric flow rate decreases here with increasing the Brownian motion parameter.
- Local skin-friction coefficient shows a noticeable increment with increasing thermophoresis parameter whereas it manifests in a strong decrement by increasing the Brownian motion parameter for both obstructed arterial regions i.e. stenosis and aneurysm at inner wall as well as at the outer wall.
- The Nusselt number shows the opposite behaviour to local skin-friction coefficient as it decreases with increasing the thermophoresis parameter and increases with greater values of Brownian motion parameter.
- The pressure distribution increases in the porous region with increasing thermophoresis parameter in both the stenosis and aneurysm section. Pressure also shows noticeable increment in the core region with increasing thermophoresis parameter.
- The nanoparticle concentration shows a decrement with increasing Grashof number (Gr) and also it decreases with an elevation in solutal: thermal buoyancy ratio parameter (N).

- The velocity field increases at the stenotic region with increasing the value of Grashof number (*Gr*) whereas it is suppressed at the aneurysm location, indicating that thermal buoyancy exerts different effects at different axial locations in the arterial segment.
- The volumetric flow rate rises in the stenotic section while it decreases in the aneurysm section with higher thermal buoyancy forces i.e. with increasing Grashof number (*Gr*).
- Increasing the value of Grashof number (*Gr*), induces lower hemodynamic impedance near the inner boundary whereas at the outer boundary (wall) there is a higher resistance in the core region of the diseased.
- The study has been motivated by applications in novel nanofluid drug delivery systems.
- This study also signify the potential of rheological properties of the blood in the blood vessel during the two crucial cardiovascular diseases (i. e., stenosis and aneurysm).

In the current analysis, shape factor effects of the nanoparticles have been ignored. Furthermore, specific nano-particle materials have been neglected since this is not possible with the Buongiorno model and revised Buongiorno model. Future studies will therefore employ the Tiwari-Das nanoscale model [57] which allows specific thermal conductivity, viscosity and heat capacity values to be computed for specific nano-particles (e.g. gold, iron oxide) and also enables different geometrical configurations to be studied via a shape factor model [78]. Additionally, in the present study attention has been confined to rigid wall arterial vessels. The deformability of blood vessels is also an important consideration [79] and this requires modification of the present model to include fluid-structure interaction (FSI) effects. The results of efforts in these directions will be communicated imminently, and it is envisaged that they will provide a deeper understanding of nano-drug fate and impact in the treatment of cardiovascular disease.

The potential application of numerical blood flow simulation is to aid decision-making processes during the treatment of cardiovascular diseases, for example, stenoses and aneurysms. Although a conventional method for treating a stenosis or aneurysm is to deploy a stent or coiling of wire and catheter, the modern trend is increasingly now to deploy nanodrugs within a particular targeted environment. The resulting modification of the flow field triggers the process of blood clotting at the stenosis and inside the aneurysm and the effect of these post-treatment processes can be predicted by computational simulation.

Acknowledgements

The authors are grateful to the Science and Engineering Research Board (SERB), Department of Science and Technology (DST), Govt of India for undertaking the research work under the research project File Number: ECR/2017/001053 dated 12/03/2018.

REFERENCES

[1] Mishra, B. K. "A Mathematical model for the analysis of blood flow in arterial stenosis, *The Mathematics Education*, vol." *XXXVII, No. IV* (2003): 176-181.

[2] Chakravarty, S., and P. K. Mandal. "Mathematical modelling of blood flow through an overlapping arterial stenosis." *Mathematical and computer modelling* 19, no. 1 (1994): 59-70.

[3] Gupta, Rajeev, Indu Mohan, and Jagat Narula. "Trends in coronary heart disease epidemiology in India." *Annals of Global Health* 82, no. 2 (2016): 307-315.

[4] Merrill, Edward W. "Rheology of human blood and some speculations on its role in vascular homeostasis." *Biomechanical Mechanisms in Vascular Homeostasis and Intravascular Thrombosis, PN Sawyer, ed., Appleton-Century-Crofts, New York* (1965): 121-137.

[5] Taylor, M. G., The influence of the anomalous viscosity of blood upon its oscillatory flow. *Physics in Medicine & Biology*, **3**, no. 3: 273, 1959.

[6] Schmid-Schönbein, Geert W., Shunichi Usami, Richard Skalak, and Shu Chien. "The interaction of leukocytes and erythrocytes in capillary and postcapillary vessels." *Microvascular Research* 19, no. 1 (1980): 45-70.

[7] Vasu, B., Ankita Dubey and O. Anwar Bég. "Finite element analysis of non-Newtonian magnetohemodynamic flow conveying nanoparticles through a stenosed coronary artery." *Heat Transfer—Asian Research* (2019):1-34. **https://doi.org/10.1002/htj.21598**

[8] Bluestein D, Niu L, Schoephoerster R T and Dewanjee M K 1997 Fluid mechanics of arterial stenosis: relationship to the development of mural thrombus. *Annals of Biomedical Engineering* 25(2): 344–356

[9] Young D F and Tsai F Y 1973 Flow characteristics in models of arterial stenoses II: unsteady flow. *J. Biomechanics* 6(5): 547–559.

[10] Reddy J V R, Srikanth D and Murthy S K 2014 Mathematical modelling of couple stresses on fluid flow in constricted tapered artery in presence of slip velocity-effects of catheter. *Applied Mathematics and Mechanics* 35(8): 947–958.

[11] Agrawal V, Paul C, Das M K and Muralidhar K 2015 Effect of coil embolization on blood flow through a saccular cerebral aneurysm. *Sadhana* 40(3): 875–887.

[12] Priyadharshini S and Ponalagusamy R 2017 Computational model on pulsatile flow of blood through a tapered arterial stenosis with radially variable viscosity and magnetic field. *Sadhana*, 42(11): 1901–1913.

[13] Baieth, HE Abdel, Physical parameters of blood as a non-Newtonian fluid. *Int. J. Biomedical Science: IJBS* **4**, no. 4: 323, 2008.

[14] Thiriet M., *Biomathematical and Biomechanical Modelling of the Circulatory and Ventilatory Systems. Vol 2: Control of Cell Fate in the Circulatory and Ventilatory Systems*. Springer Math& Biological Modelling, New York, USA, 2011.

[15] Riahi, D. N., Roy, R. and Cavazos, S., On arterial blood flow in the presence of an overlapping stenosis. *Mathematical and Computer Modelling*. **54**. 2999-3006, 2011.

[16] Chakravarty, Santabrata, and Mandal Prashanta Kumar, Two-dimensional blood flow through tapered arteries under stenotic conditions. *International Journal of Non-Linear Mechanics*, **35**, no. 5: 779-793, 2000.

[17] Mekheimer, K.S. and El Kot, M.A., Mathematical modelling of unsteady flow of a Sisko fluid through an anisotropically tapered elastic arteries with time-variant overlapping stenosis. *Applied Mathematical Modelling*, **36**(11), 5393-5407, 2012.

[18] Akbar, NS, Nadeem S. and M. Ali., Jeffrey fluid model for blood flow through a tapered artery with a stenosis. *Journal of Mechanics in Medicine and Biology* 11, 03: 529-545, 2011.

[19] Ellahi, R., Rahman, S. U, Gulzar, M., Nadeem, S., and Vafai, K., A mathematical study of non-Newtonian micropolar fluid in arterial blood flow through composite stenosis, *Applied Mathematics & Information Sciences.* **4**. 1567–1573, 2014.

[20] Razavi, A., Shirani, E., and Sadeghi, M. R. (2011). Numerical simulation of blood pulsatile flow in a stenosed carotid artery using different rheological models. *J. Biomech*.44,2021–2030.

[21] Karimi, S., Dadvar, M., Dabagh, M., Jalali,P., Modarress, H., and Dabir, B. (2013). Simulation of pulsatile blood flow through stenotic artery considering different blood rheologies: comparision of 3D and 2D- axisymmetric models. *Biomed. Eng. Appl. Basis Commun*. 25, 1350023.

[22] Nadeem, S., and S. Ijaz. "Influence of metallic nanoparticles on blood flow through arteries having both stenosis and aneurysm." *IEEE Transactions on Nanobioscience* 14, no. 6 (2015): 668-679.

[23] Mukhopadhyay, Swati, and G. C. Layek. "Analysis of blood flow through a modelled artery with an aneurysm." *Applied Mathematics and Computation* 217, no. 16 (2011): 6792-6801.

[24] B. V. R. Kumar and K. B. Naidu, "Finite element analysis of nonlinear pulsatile suspension flow dynamics in blood vessels with aneurysm", *Comp. Biol. Med*., vol. 25, pp 1-20, 1995.

[25] Bluestein, D., L. Niu, R. T. Schoephoerster, and M. K. Dewanjee. "Steady flow in an aneurysm model: correlation between fluid dynamics and blood platelet deposition." *ASME J. Biomechanical Engineering*, 118, no. 3 (1996): 280-286.

[26] N. Casson, "Rheology of disperse systems," in *Flow Equations for Pigment Oil Suspensions of the Printing Ink Type. Rheology of Disperse Systems, C. C. Mill, Ed.*, pp. 84–102, Pergamon Press, London, UK (1959).

[27] Chakravarty, Santabrata, and Prashanta Kumar Mandal. "Numerical simulation of Casson fluid flow through differently shaped arterial stenoses." *Zeitschrift für angewandte Mathematik und Physik* 65, no. 4 (2014): 767-782.

[28] G. W. S. Blair, “An equation for the flow of blood, plasma and serum through glass capillaries”, *Nature*, vol.183, no. 4661, pp. 613–614, 1959.

[29] A. L. Copley, “Apparent viscosity and wall adherence of blood systems,” in *Flow Properties of Blood and Other Biological Systems, A. L. Copley and G. Stainsly, Eds*., Pergamon Press, Oxford,UK,1960.

[30] Haghighi, A. R., & Chalak, S. A., Mathematical modelling of blood flow through a stenosed artery under body acceleration. *Journal of the Brazilian Society of Mechanical Sciences and Engineering*, **39**(7), 2487-2494, 2017.

[31] A. Zaman, N. Ali, O. Anwar, Numerical study of unsteady blood flow through a vessel using Sisko model, JESTECH. (2015).

[32] Mekheimer, K.S. and El Kot, M.A., Mathematical modelling of unsteady flow of a Sisko fluid through an anisotropically tapered elastic arteries with time-variant overlapping stenosis. *Applied Mathematical Modelling*, **36**(11), 5393-5407, 2012.

[33] N. Ali, A. Zaman, M. Sajid, Unsteady blood flow through a tapered stenotic artery using Sisko model, Computers and Fluids 101 (2014) 42-49.

[34] R. Baliand U. Awasthi, “Mathematical model of blood flow in the small blood vessel in presence of magnetic field,” Applied Mathematics, vol.2, pp.264–269, 2011.

[35] Mishra, S., Siddiqui S.U. and Medhavi, A., Blood flow through a composite stenosis in an artery with permeable wall, *Applications and Applied Mathematics*. **6(1)**. 1798-1813, 2011.

[36] M. Jain, G.C. Sharma, and R. Singh, “Mathematical modelling of blood flow in a stenosed artery under MHD effect through porous medium,”International Journal of Engineering, Transactions B, vol.23, no.3-4, pp.243–251, 2010.

[37] D. Tripathi, “A mathematical model for blood flow through an inclined artery under the influence of an inclined magnetic field,”Journal of Mechanics in Medicine and Biology, vol.12, pp. 1–18, 2012.

[38] I. M. Eldesoky, “Slip effects on the unsteady MHD pulsatile Blood flow through porous medium in an artery under the effect of body acceleration, ”International Journal of Mathematics and Mathematical Sciences, vol. 2012, Article ID860239, 26 pages,2012.

[39] Srivastav, R. K., Mathematical model of blood flow through a composite stenosis in catheterized artery with permeable wall, *Applications and Applied Mathematics.* **99.** 58–74, 2014.

[40] Choi, S. U. S., and J. A. Eastman, Enhancing thermal conductivity of fluids with nanoparticles, *ASME-Publications-Fed* 231: 99-106, 1995.

[41] Buongiorno, J., Convective transport in nanofluids. ASME J. Heat Transfer, 128, 3: 240-250, 2006.

[42] Kuznetsov, A. V., and D. A. Nield. "Natural convective boundary-layer flow of a nanofluid past a vertical plate: A revised model." *International journal of thermal sciences* 77 (2014): 126-129.

[43] Ray, Atul Kumar, Buddakkagari Vasu, O. Anwar Bég, Rama SR Gorla, and P. V. S. N. Murthy. "Homotopy semi-numerical modeling of non-Newtonian nanofluid transport external to multiple geometries using a revised Buongiorno Model." *Inventions* 4, no. 4 (2019): 54.

[44] Das, S.K., S.U. Choi, W. Yu and T. Pradeep, Nanofluids: Science and Technology, CRC Press, USA, 416pp, 2007.

[45] Masuda, Hidetoshi, Akira Ebata, and Kazumari Teramae., Alteration of thermal conductivity and viscosity of liquid by dispersing ultra-fine particles. Dispersion of Al2O3, SiO2 and TiO2 ultra-fine particles, *Netsu Bussei*, **7**, 227-233, 1993.

[46] Farooq, Muhammad, M. Ijaz Khan, M. Waqas, T. Hayat, A. Alsaedi, and M. Imran Khan. "MHD stagnation point flow of viscoelastic nanofluid with non-linear radiation effects." *Journal of molecular liquids* 221 (2016): 1097-1103.

[47] Hayat, Tasawar, Muhammad Waqas, Muhammad Ijaz Khan, and Ahmed Alsaedi. "Analysis of thixotropic nanomaterial in a doubly stratified medium considering magnetic field effects." *International Journal of Heat and Mass Transfer* 102 (2016): 1123-1129.

[48] Ahmadi, Mohammad Hossein, Amin Mirlohi, Mohammad Alhuyi Nazari, and Roghayeh Ghasempour. "A review of thermal conductivity of various nanofluids." *Journal of Molecular Liquids* 265 (2018): 181-188.

[49] Waqas, M., M. Ijaz Khan, T. Hayat, and A. Alsaedi. "Stratified flow of an Oldroyd-B nanoliquid with heat generation." *Results in physics* 7 (2017): 2489-2496.

[50] Hayat, T., M. Ijaz Khan, M. Waqas, A. Alsaedi, and Muhammad Imran Khan. "Radiative flow of micropolar nanofluid accounting thermophoresis and Brownian moment." *International Journal of Hydrogen Energy* 42, no. 26 (2017): 16821-16833.

[51] Wong KFV, Bon BN, Vu S, Samedi S, Study of nanofluid natural convection phenomena in rectangular enclosures, *ASME International Mechanical Engineering Congress and Exposition (IMECE '07), vol. 6, pp. 3–13, Seattle, Wash, November*, 2007.

[52] O. Anwar Bég, M.M. Rashidi, M. Akbari, A. Hosseini, Comparative numerical study of single phase and two-phase models for bio-nanofluid transport phenomena, *J. Mechanics in Medicine and Biology*, 14, 1450011.1-31, 2014.

[53] M. J. Uddin, M.N. Kabir, O. Anwar Bég and Y. Alginahi, Chebyshev collocation computation of magneto-bio convection nanofluid flow over a wedge with multiple slips and magnetic induction, *Proc. IMechE: Part N-Journal of Nanomaterials, Nanoengineering and Nanosystems* (2018). doi: 10.1177/2397791418809795 (15 pages).

[54] S.A.A. Rizvi and A.M. Saleh, Applications of nanoparticle systems in drug delivery technology, *Saudi Pharmaceutical J.,* 26(1): 64–70, 2018.

[55] P. H. da Costa Santos, Development of a biodegradable nanofluid for brain drug delivery, *Master Science in Biomedical Engineering, University of Coimbra, Portugal, September* (2015).

[56] N. S. Akbar, D. Tripathi and O. Anwar Bég, Variable-viscosity thermal hemodynamic slip flow conveying nanoparticles through a permeable-walled composite stenosed artery, *European Physical Journal Plus,* 132: 294 -305, 2017.

[57] O. Anwar Bég, Nonlinear multi-physical laminar nanofluid bioconvection flows: Models and computation, *A. Sohail, Z. Li (Eds.): Computational Approaches in Biomedical Nano-Engineering, Wiley,* Chapter 5, pp. 113-145 (2018).

[58] Y. Yan *et al*., Euryale ferox seed-inspired super-lubricated nanoparticles for treatment of osteoarthritis, *Adv. Functional Materials*, 29 (4), 1807559, 2019.

[59] M.M. Raj Sha et al., Ultra-pure silicon nanofluid by laser ablation: thermal diffusivity studies using thermal lens technique, *Applied Physics B,* 124: 213, 2018.

[60] D. Tripathi, A. Sharma and O. Anwar Bég, Electrothermal transport of nanofluids via peristaltic pumping in a finite micro-channel: *effects of Joule heating and Helmholtz-Smoluchowski velocity, Int. J. Heat Mass Transfer,* 111, 138–149, 2017.

[61] M. Karimi *et al.,* "Nanotechnology in diagnosis and treatment of coronary artery disease." *Nanomedicine* 11, no. 5 (2016): 513-530.

[62] Rhee, June-Wha, and Joseph C. Wu. "Advances in nanotechnology for the management of coronary artery disease." *Trends in Cardiovascular Medicine* 23, no. 2 (2013): 39-45.

[63] Giljohann, David A., Dwight S. Seferos, Weston L. Daniel, Matthew D. Massich, Pinal C. Patel, and Chad A. Mirkin., Gold nanoparticles for biology and medicine. *Angewandte Chemie International Edition* **49**, no. 19: 3280-3294, 2010.

[64] Kumar, K. Praveen, Willi Paul, and Chandra P. Sharma., Green synthesis of gold nanoparticles with Zingiber officinale extract: characterization and blood compatibility, *Process Biochemistry* **46**, no. 10: 2007-2013, 2011.

[65] Ali, N., Zaman A., Sajid M., Bég, Anwar O., Shamshuddin M. D. and Ali Kadir., Numerical simulation of time-dependent non-Newtonian nano-pharmacodynamic transport phenomena in a tapered overlapping stenosed artery, *Nanoscience and Technology: An International Journal,* **9**, 247-282, 2018.

[66] Bali, R. and U. Awasthi. "A Casson fluid model for multiple stenosed artery in the presence of magnetic field." *Applied Mathematics* 3, no. 05 (2012): 436.

[67] I.Wang and J.F.Stoltz, Influence of non-Newtonian properties of blood on the global transport of red blood cells. *Clinical Hemorheology*, 14 (1994),789–796.

[68] Hecht, Frederic, New development in FreeFEM++, *J. Numerical Mathematics,* **20**, 251-266, 2012.

[69] Sauvage, Emilie, Patient-specific blood flow modelling, *Ph. D. Thesis, Université Catholique de Louvain, Belgium*, 2014.

[70] K.J. Bathe, Finite Element Procedures, Prentice-Hall, New York, USA (1996).

[71] O. Anwar Bég, Numerical methods for multi-physical magnetohydrodynamics, Chapter 1, pp. 1-112, *New Developments in Hydrodynamics Research, M. J. Ibragimov and M. A. Anisimov, Eds*., Nova Science, New York, USA, *2012.*

[72] Dubey A, and Vasu B., Finite element analysis of MHD blood flow in stenosed coronary artery with the suspension of nanoparticles, *Springer Nature*, 2019.

[73] Ellahi, R., S. U. Rahman, S. Nadeem, and Noreen Sher Akbar. "Blood flow of nanofluid through an artery with composite stenosis and permeable walls." *Applied Nanoscience* 4, no. 8 (2014): 919-926.

[74] K. Park, Nanotechnology: What it can do for drug delivery, *J. Control Release*, 120, 1-3, 2007.

[75] Shen Y, Tang H, Zhan Y, Van Kirk EA, Murdoch WJ., Degradable poly (beta-amino ester) nanoparticles for cancer cytoplasmic drug delivery. *Nanomedicine Nanotechnol Biol Med*. 5(2):192–201, 2009.

[76] Chen M. M. and Holmes K. R. "Microvascular Contributions in Tissue Heat Transfer", *Ann. N.Y. Acad. Sci.*, 0077-8923, 335, pp. 137-151, 1980.

[77] A. Schitzer and R. C. Eberhart, (eds.), "*Heat Transfer in Medicine and Biology",* Plenum Press, New York, Vol. II (1985).

[78] N. S. Akbar, D. Tripathi and O. Anwar Bég, Modelling nanoparticle geometry effects on peristaltic lumping of medical magnetohydrodynamic nanofluids with heat transfer, *J. Mechanics in Medicine and Biology,* 16 (2) 1650088.1-1650088.20, 2015.

[79] N. Elabbasi and K.-J. Bathe, Some advances in modelling multi-physics-biomedical applications, *Second MIT Conference on Computational Fluid and Solid Mechanics, MIT, USA, June* (2003).